Department of Precision and Microsystems Engineering

An interface-enriched finite element method for electromagnetic analysis and optimization of 2D problems

Steven van Bergen

Report no : 2022.081
Coach : Dr. R. A. Norte, Dr. A. M. Aragón
Specialisation : Engineering Dynamics & Engineering Mechanics
Type of report : Master Thesis
Date : November 25th, 2022

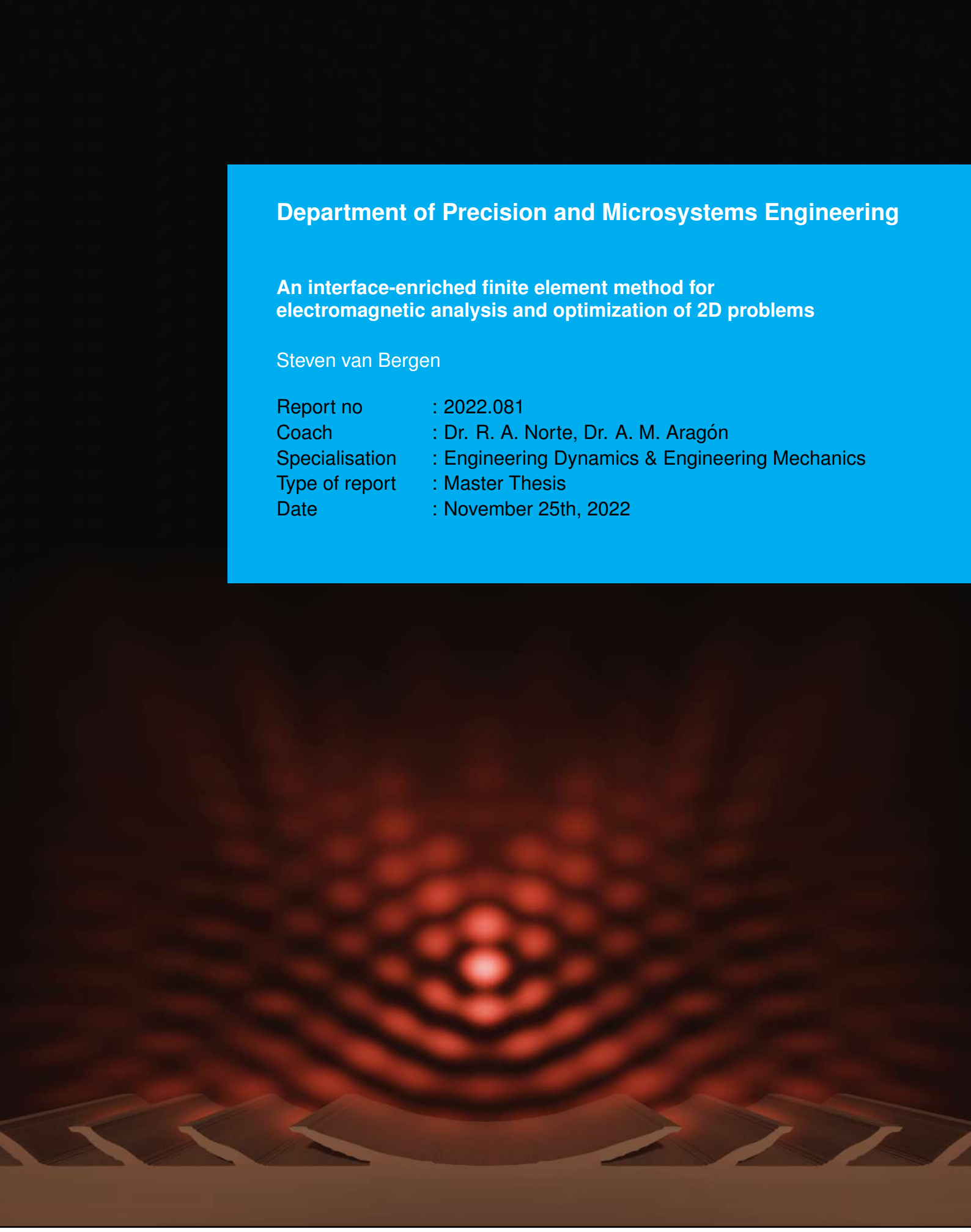

TU Delft Delft University of Technology

Challenge the future

An interface-enriched finite element method for electromagnetic analysis and optimization of 2D problems

Steven van Bergen
4585933

Supervisors:
Dr. A. M. Aragón
Dr. R. A. Norte

Master thesis submitted to Delft University of Technology in partial fulfilment of the requirements for the degree of Master of Science in Mechanical Engineering
Faculty of Mechanical, Maritime and Materials Engineering
Technical University of Delft
The Netherlands

Abstract

Nanophotonics is the study of structures' interaction with light with features at or below the nanometer scale. It has gained the interest of many researchers, as it can be used to control the flow of light very effectively in the design of, *e.g.*, solar cells, highly efficient biosensors or lasers. The design of such devices can be non-intuitive and complex and therefore computational tools like topology optimization techniques have been used to improve their designs. However, the topology optimization methods used in the literature often use a density-based representation of the geometry, which often leads to jagged edges. It has been shown in the literature that jagged edges can deteriorate the accuracy of simulation results. Using a level set method in combination with an enriched finite element method offers a smoother boundary representation than the often used density-based methods. This work aims to develop an analysis and level set optimization for 2D electromagnetic scattering and eigenvalue problems using an enriched finite element method. Furthermore, we showcase that even for a non-conforming discretization, the enriched finite element method achieves the same convergence properties as the standard finite element method with fitted meshes. Finally, we perform topology optimization on the design of both a 2D meta lens and 2D reflector, maximizing their ability to focus light onto a point, using a level set method to define the geometry in combination with the enriched method used in the analysis.

Contents

1

Introduction

Over the last two decades the advancements in fabrication capabilities, which allowed for the manufacturing of structures at the micro- and nano-scales, has caused a rise of interest in nanophotonics—the study of structures' interaction with light with features at or below the nanometer scale [1]. Structures at this length scale can be used to control the flow of light in new ways that were not possible before [2]. Nanophotonics has already found many potential applications such as solar cells [3], highly efficient lasers [4, 5], biosensors [6–8], and the treatment or detection of diseases [9, 10]. Most of these applications use a photonic crystal, which is an optical material that uses periodic structures causing interference of light, also known as Bragg scattering, to create frequency bands in which light is attenuated, also known as band gaps [11]. Using this, defects inside of this periodic structure can be used to guide, confine or filter the flow light very effectively. Using photonic crystals in the design of nanophotonics can be non-intuitive, hence why optimization, which is a design strategy where the material layout in a defined space is optimized to achieve a design with better performance, has been a prevalent tool in nanophotonics. During optimization, an objective function, which represents the figure of merit, is maximized or minimized. Commonly, constraints are introduced to ensure that the designs are feasible. A common optimization technique, parametric optimization [12–15], has been used for optimizing the dimensions or shape for certain features of traditional designs. However, they can only explore a limited range of designs, for which we do not know if their performance is anywhere near the optimal performance. Moreover, for some aspects in nanophotonics, for example multi-frequency applications or nonlinear phenomena, intuition-based design techniques becomes increasingly more difficult to apply [1]. A less constrained optimization method, shape optimization, has also been applied to optimization nanophotonic devices [5, 16]. However, the commonly used photonic crystal structures present in nanophotonic devices, which often contain many holes, are difficult to design for using shape optimization since the topological properties must stay the same limiting the design space.

By using topology optimization, which allows for the nucleation of holes inside the domain, we can freely change the material distribution for more complex and and non-intuitive designs. Various methods have been proposed in order to represent the material distribution inside of the domain. In the commonly used density-based approaches a density value is used for each element in the discretization, which is usually considered to be continuously between zero and one interpolating the properties of the design material. The intermediate densities do not correspond to a realistic material which is why a penalization scheme can be applied to make the intermediate values unfavorable for the optimizer, although they already seem to be unfavorable in problems where large reflections are desired [17]. Occasionally, a threshold filter is added to the design, creating so-called black-and-white designs without any intermediate densities [18, 19]. Density-based topology optimization has been used for the design of *e.g.*, photonic crystal band gaps [20], resonant cavities [21–24], waveguides [25–27], and photonic crystal modes with Dirac-like cones [28]. However, a disadvantage of this approach is the mesh dependency of the geometry, *i.e.*, every topology must conform to the edges of the original finite element mesh. Material interfaces that are not aligned with element edges can only be represented with a

jagged edge or interpolated values, which have shown to deteriorate the accuracy band structure computation in phononics [29]. Also, it has been shown that random spatial variations in photonic crystal structures simulations, which might be similar to the jagged edges in a density-based approach, can have a large impact on the efficiency of confinement and guiding of light [30–32]. This shows that it is important to choose a method that can accurately model material interfaces during the optimization of nanophotonic devices.

To reduce the mesh dependency on the material distribution, a level set function could be used whose zero contour delineates the material interfaces, resulting in smoother and distinct interfaces. Although a level set might always have a clear boundary, it still needs to be projected to the finite element mesh when doing analysis which can result in intermediate densities. This issue can be solved by using an enriched finite element method that adds enrichments at material boundaries, *i.e.*, one can enrich cut elements by adding enrichment functions on top of the standard finite element formulation (h-FEM) to represent the material interface with an unfitted mesh. Examples of such methods is the eXtended/Generalized FEM (X/GFEM) [33, 34], which can handle both strong and weak discontinuities—discontinuities in the field itself or in its gradient, respectively. X/GFEM has been used for electromagnetic analysis [35–39] and to optimize a magnetic actuator [40]. However, using X/GFEM introduces some challenges, *e.g.*, prescribing interface conditions or essential boundary conditions need special formulations [41, 42]. Moreover, the shape function need to be chosen carefully as they could degrade the accuracy of the method [41]. In the view of these limitations, the Interface-enriched Generalized FEM (IGFEM) [43, 44] presents a viable solution to these problems. Instead of adding enrichments to element nodes, in IGFEM the enrichments are assigned to new nodes that are created along the discontinuities. The enriched nodes enhance the original nodal field with enriched shape functions, which vanish at the nodes of the original mesh causing the original nodes to keep its physical meaning. IGFEM has already been applied to the analysis [45, 46] and parametric optimization [47] of electromagnetic problems using edge elements and showed promising results. The level set-based optimization using IGFEM by moving the enriched nodes with the material interface every iteration has been applied to optimize for compliance [48] and phononic band gap optimization [29], but not yet to electromagnetic problems.

In this thesis, we propose a 2D IGFEM-based analysis in combination with a level set based topology optimization method, based on the methods presented in van den Boom et al. [48], to perform nanophotonic design with a clean material boundary representation [48]. Contrasting with the work of Zhang et al. [47], where the degrees of freedom are assigned to the edges of finite elements (edge elements), in this work we assign the degrees of freedom to the nodes of finite elements (nodal elements) [47]. Using the standard finite element formulation with nodal elements can sometimes result in spurious solutions because the divergence conditions, which usually do not appear explicitly in the system equations, are not satisfied [49]. Edge elements are commonly used in this situation because they always satisfy the divergence conditions [50, 51]. However, the 2D formulation of Maxwell's equations, where only the out-of-plane electric and magnetic fields are solved, can be handled by the standard finite element formulation without the use of edge elements, as there will only be weak discontinuities [49]. Thus using nodal elements is still valid in this case with the added benefit of being easier to implement. First, a 2D IGFEM-based electromagnetic analysis is proposed for harmonic scattering and eigenvalue problems. Next, a band structure analysis is performed on photonic crystal designs taken from Joannopoulos et al. [11] using h-FEM and IGFEM [11]. Furthermore, a convergence analysis is performed on a simple Mie scattering problem for h-FEM and IGFEM, demonstrating a optimal convergence rate for both. At last, we formulate the optimization problem taken from Christiansen and Sigmund [52] for maximizing light intensity concentration and use it to design a meta lens and a reflector, yielding similar design as in the literature [52].

2

An interface-enriched finite element method for electromagnetic analysis and optimization of 2D problems

The first part of this section will elaborate on the formulation of the analysis which can be used for band structure and scattering analysis. Also, a level set optimization for electromagnetic problems using IGFEM will be described. The second part will present three example problems to verify the implementation of the analysis and optimization. The final section contains a short conclusion and discussion of the results.

2.1 Simulation

The simulation domain Ω, shown on the right in Fig. 1, is composed of a dielectric domain Ω_d and a vacuum domain Ω_v such that $\overline{\Omega} = \overline{\Omega}_\mathrm{d} \cup \overline{\Omega}_\mathrm{v}$ and $\Omega_\mathrm{d} \cap \Omega_\mathrm{v} = \emptyset$. We assume there to be no sources inside of the domain, meaning the electric current density ($\mathbf{J}$) is zero. Finally, the interface between the dielectric and vacuum domain, defined by a level set function ϕ, is denoted by Γ^i and the outer boundary is denoted by Γ^o.

The electromagnetic boundary value problem in strong form can be formulated with the time-harmonic Maxwell's equations [49]:

$$\nabla \times \mathbf{E} = -j\omega\mathbf{B} \qquad \text{in } \Omega, \tag{1}$$

$$\nabla \times \mathbf{H} = j\omega\mathbf{D} \qquad \text{in } \Omega, \tag{2}$$

$$\nabla \cdot \mathbf{D} = 0 \qquad \text{in } \Omega, \tag{3}$$

$$\nabla \cdot \mathbf{B} = 0 \qquad \text{in } \Omega, \tag{4}$$

where $\mathbf{E}$ and $\mathbf{H}$ are the electric and magnetic fields, $\mathbf{D}$ and $\mathbf{B}$ are the electric and magnetic flux density, ω is the frequency and j is the complex number. At the interface of two different materials,

the interface conditions need to be satisfied

$$\hat{n} \times (\mathbf{E}_1 - \mathbf{E}_2) = 0 \qquad \text{on } \Gamma^i, \tag{5}$$
$$\hat{n} \cdot (\mathbf{D}_1 - \mathbf{D}_2) = 0 \qquad \text{on } \Gamma^i, \tag{6}$$
$$\hat{n} \times (\mathbf{H}_1 - \mathbf{H}_2) = 0 \qquad \text{on } \Gamma^i, \tag{7}$$
$$\hat{n} \cdot (\mathbf{B}_1 - \mathbf{B}_2) = 0 \qquad \text{on } \Gamma^i. \tag{8}$$

The variables in these equations are independent of time because the harmonic component in the form of a complex potential can be suppressed. For linear and isotropic media, the following constitutive relations hold [53]:

$$\mathbf{D} = \epsilon \mathbf{E}, \tag{9}$$
$$\mathbf{B} = \mu \mathbf{H}, \tag{10}$$

where ϵ is the permittivity and μ is the permeability. These can be defined by

$$\epsilon = \epsilon_r \epsilon_0, \tag{11}$$
$$\mu = \mu_r \mu_0, \tag{12}$$

where ϵ_r and μ_r are called the relative permittivity and permeability. These constants are taken relative to the vacuum permittivity and permeability, which are denoted by ϵ_0 and μ_0. Substituting (9) and (10) into (1) and (2) respectively yields:

$$\frac{1}{\mu} \nabla \times \mathbf{E} = -j\omega \mathbf{H} \qquad \text{in } \Omega, \tag{13}$$
$$\frac{1}{\epsilon} \nabla \times \mathbf{H} = j\omega \mathbf{E} \qquad \text{in } \Omega, \tag{14}$$

Taking the curl of (13) and substituting (2) to eliminate $\mathbf{H}$ yields

$$\nabla \times \left(\frac{1}{\mu_r} \nabla \times \mathbf{E} \right) - \epsilon_r \left(\frac{\omega}{c} \right)^2 \mathbf{E} = 0 \qquad \text{in } \Omega, \tag{15}$$

and doing the same procedure for (14) with respect to $\mathbf{H}$ gives

$$\nabla \times \left(\frac{1}{\epsilon_r} \nabla \times \mathbf{H} \right) - \mu_r \left(\frac{\omega}{c} \right)^2 \mathbf{H} = 0 \qquad \text{in } \Omega. \tag{16}$$

These equations are called the vector wave equations. Both can be used to solve for an eigenvalue problem where ω is the unknown eigenvalue and $\mathbf{E}$ or $\mathbf{H}$ the unknown eigenvector. Eigenvalue analysis is often used within nanophotonics to perform band structure analysis on a photonic crystal, which shows the frequencies of the eigenmodes for all propagation directions and wavelengths, defined by the wave vector k. This can be used to find the band gaps created by periodic photonic crystal structures. If ω is known, the vector wave equation is turned into a scattering problem where $\mathbf{E}$ or

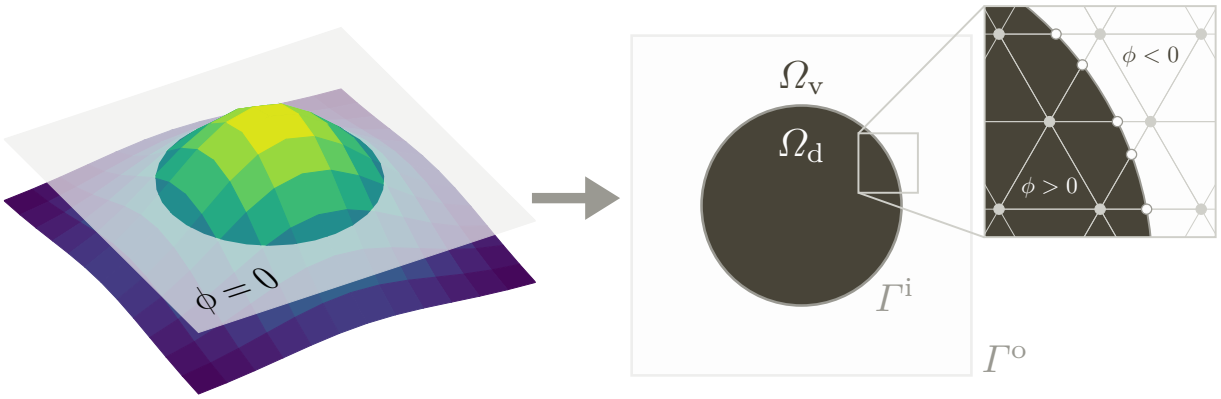

Fig. 1: An illustration of the simulation domain using IGFEM showing a dielectric Ω_d with material interface Γ^i, defined by a level set function ϕ. The dielectric is surrounded by a vacuum Ω_v and outer boundary Γ^o. The inset shows the discretization around the material interface that is non matching to the mesh. Here, the grey nodes ● represent the original mesh nodes and the white nodes ○ represent enriched nodes.

H are the resulting electric and magnetic field, respectively. For 2D problems, where we assume no variations in the medium and fields with respect to the z direction, (15) and (16) can be rewritten to the inhomogeneous scalar vector wave equations

$$\left[\frac{\partial}{\partial x}\left(\frac{1}{p}\frac{\partial}{\partial x}\right)+\frac{\partial}{\partial y}\left(\frac{1}{p}\frac{\partial}{\partial y}\right)+q\left(\frac{\omega}{c}\right)^2\right]u=0 \qquad \text{in } \Omega, \tag{17}$$

where for out-of-plane polarization for the electric field, $u=E_z$, $p=\mu_r$ and $q=\epsilon_r$ and for in-plane polarization of the electric field, $u=H_z$, $p=\epsilon_r$ and $q=\mu_r$. The out-of-plane and in-plane polarizations for the electric field are also known as Transverse Magnetic (TM) and Transverse Electric (TE) polarization respectively.

The weak form of (17) can be written as

$$\sum_{i=\mathrm{d,v}}\int_{\Omega_i}\frac{1}{p_i}\frac{\partial v_i}{\partial x}\frac{\partial u_i}{\partial x}+\frac{1}{p_i}\frac{\partial v_i}{\partial y}\frac{\partial u_i}{\partial y}\mathrm{d}\Omega+\omega^2\sum_{i=\mathrm{d,v}}\int_{\Omega_i}\frac{q_i}{c^2}v_iu_i\,\mathrm{d}\Omega=0 \qquad \forall v\in\mathcal{V}_0, \tag{18}$$

The trial function v_i and weight function u_i are both taken from the function space

$$\mathcal{V}_0=\left\{v\in\mathcal{L}^2(\Omega),\, v|_{\Omega_i}\in\mathcal{H}^1\left(\Omega_i\right),\, v|_{\Gamma_i^{\mathrm{D}}}=0, i=\mathrm{d,v}\right\}, \tag{19}$$

where $\mathcal{L}^2(\Omega)$ is the space of square-integrable functions and $\mathcal{H}^1\left(\Omega_i\right)$ is the first-order Sobolev space.

The discretization of the domain when using IGFEM is done without any knowledge of the material distribution inside of the domain. The set of nodes of the original mesh will be assigned to standard Lagrangian shape functions. Next, a level set function $\phi(\boldsymbol{x})$ is used to define the material interfaces where its sign corresponds to the dielectric and vacuum domains. By placing new enriched nodes at the intersection of the zero contour of the level set function and element edges of the original mesh, the material interfaces can be resolved properly. This process is shown in Fig. 1. The location of these enriched nodes $\boldsymbol{x}_n$ can be found by

$$\boldsymbol{x}_n=\boldsymbol{x}_j-\frac{\phi(\boldsymbol{x}_j)}{\phi(\boldsymbol{x}_k)-\phi(\boldsymbol{x}_j)}(\boldsymbol{x}_k-\boldsymbol{x}_j), \tag{20}$$

which is the linear interpolation of the level set function between the supporting nodes $\boldsymbol{x}_k$ and $\boldsymbol{x}_j$ on the intersected edge from the original mesh [48]. The degrees of freedom corresponding to the enriched node will then be assigned to an enriched shape function, shown in Fig. 2, which is then added to the original formulation. The elements that are cut by a material interface are subdivided into smaller elements such that the change of material can be properly represented while not changing the underlying mesh. Following a Bubnov–Galerkin approach, the IGFEM approximation can then be written as [48]

$$u^h(\boldsymbol{x})=\underbrace{\sum_{i\in\iota_h}N_i(\boldsymbol{x})U_i}_{\text{standard FEM}}+\underbrace{\sum_{i\in\iota_w}s_i\psi_i(\boldsymbol{x})\alpha_i}_{\text{enrichment}}, \tag{21}$$

where u^h is the approximated solution and ι_h and ι_w are the index sets corresponding to the original and enriched nodes respectively. The first term consists of the standard finite element formulation—the superposition of the shape functions $N_i(\boldsymbol{x})$ multiplied by the corresponding degrees of freedom U_i for every node in ι_h. The second term consists of the enriched finite element formulation—the superposition the weakly discontinuous shape functions $\psi_i(\boldsymbol{x})$ multiplied by the corresponding degrees of freedom α_i and a scaling factor s_i that helps with producing a well-conditioned system [44] for every node in ι_w.

After the domain is discretized into finite elements, (18) is integrated element wise using Gauss points. The local stiffness matrix is computed on each integration element $\boldsymbol{\xi}$ as

$$\boldsymbol{k}_e=\int j_e\boldsymbol{B}^{\mathrm{T}}\boldsymbol{D}_e(p_e)\boldsymbol{B}d\boldsymbol{\xi}, \tag{22}$$

and the local mass matrix as

$$\boldsymbol{m}_e=\int j_e\frac{q_e}{c^2}\boldsymbol{N}\boldsymbol{N}^{\mathrm{T}}d\boldsymbol{\xi}, \tag{23}$$

where $\boldsymbol{N}$ contains the values of the shape functions (and enrichment functions if the integration element is enriched) of the nodes in support of the elements, $\boldsymbol{B}$ contains their spatial derivatives and $\boldsymbol{D}_e$ is the constitutive matrix. A further explanation of these equations is given in van den Boom et al. [48]. The linear set of equations $\boldsymbol{K}\boldsymbol{U}-\omega^2\boldsymbol{M}\boldsymbol{U}=0$ is finally obtained by standard procedures

$$\boldsymbol{K}=\bigtriangleup_e\boldsymbol{k}_e, \quad \boldsymbol{M}=\bigtriangleup_e\boldsymbol{m}_e, \tag{24}$$

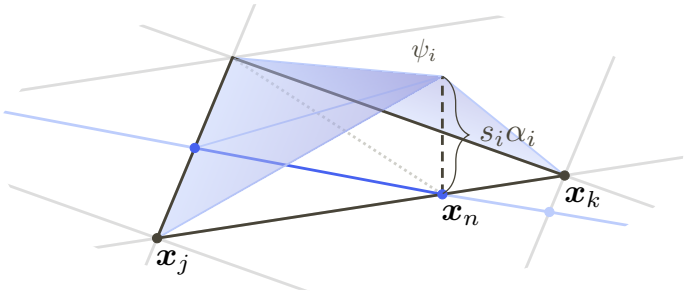

Fig. 2: A schematic of the IGFEM approximation, where $s_i\alpha_i$ is the scaled enriched DOF and ψ_i is the corresponding enrichment function, $\boldsymbol{x}_n$ is the coordinate of the enriched node and $\boldsymbol{x}_k$ and $\boldsymbol{x}_j$ are the coordinates of the supporting nodes. The discontinuity and enriched nodes are given a blue color.

where $\bigtriangleup$ denotes the standard finite element assembly process combining local element matrices into a global matrix, $\boldsymbol{K}$ and $\boldsymbol{M}$ are the global stiffness and mass matrix, $\boldsymbol{U}$ is the solution vector containing both standard and enriched degrees of freedom.

2.1.1 Periodic boundary conditions

As previously discussed a band structure analysis can be performed on a periodic photonic crystal structure to find band gaps. For this analysis it is assumed that the boundaries of the domain are periodic—the repeating element of the photonic crystal, also known as the unit cell, is repeated infinitely. To enforce this boundary condition, a Bloch-Floquet boundary condition is used on the outer boundary Γ^o of the domain connecting the fields on two opposing boundaries with the expression

$$u(\boldsymbol{x}_s) = e^{j\boldsymbol{ka}}u(\boldsymbol{x}_m), \tag{25}$$

where $\boldsymbol{a}$ is the lattice vector, which describe the spatial frequency and direction of the periodic boundary and $\boldsymbol{x}_m$ and $\boldsymbol{x}_s$ are the coordinates of a main and a subordinate node, respectively. These nodes are on either side of two connected boundaries and are separated by exactly one lattice vector $\boldsymbol{a}$. When using an enriched formulation, the enriched degrees of freedom α_i do not correspond directly to the electric or magnetic field at the location of the enriched node. Instead, the original degrees of freedom in support of the enriched node must also be taken into account as shown in (21). Substituting (21) into (25) yields

$$\alpha_s = \frac{e^{j\boldsymbol{ka}}}{s_s\psi_s(\boldsymbol{x}_s)}\left[\sum_{i\in\iota_m} N_i(\boldsymbol{x}_m)U_i + s_m\psi_m\boldsymbol{x}_m\alpha_m\right] - \frac{1}{s_s\psi_s(\boldsymbol{x}_s)}\sum_{i\in\iota_s} N_i(\boldsymbol{x}_s)U_i, \tag{26}$$

where ι_m and ι_s are the sets of main and subordinate nodes, respectively [42].

2.1.2 Symmetry conditions

Within computational electromagnetics, the Dirichlet and Neumann boundary conditions represent perfect electric or magnetic conducting surfaces depending on the polarization of the light, which are non-physical materials with infinite conductivity. In this work these types materials are not considered, however these boundary conditions can still be used as symmetry or asymmetry conditions to reduce computational time in symmetric problems. The homogeneous Dirichlet boundary condition will impose a asymmetry condition and the homogeneous Neumann boundary condition will impose a symmetry condition, for both TM and TE polarization problems [54].

2.1.3 Absorbing boundary conditions

The finite element analysis used in this work uses a limited sized domain, which has the issue of waves possibly reflecting from the outer boundary of the simulation domain and creating nonphysical results. To make sure this does not happen, an absorbing boundary condition can be used to make sure outgoing waves are attenuated before they hit the boundary. A commonly used boundary condition for attenuating outgoing waves is the absorbing boundary condition (ABC). This method exists in different orders, increasing in complexity and in efficiency as the order increases. In this work however, the absorbing boundary condition is modelled using Locally-Conformal Perfectly Matched Layers (LC-PML), as described in [55]. LC-PML adds an absorbing region Ω_{PML} at the edges of the simulation

domain such that $\Omega_{\text{PML}} \cap \Omega_d = \emptyset$, which will absorb any outgoing waves before they hit the boundary of the domain. The disadvantage of the LC-PML compared to the ABC is that the LC-PML will increase the number of unknowns because of the added space around the simulation domain. The reason of using LC-PML, however, is that it has improved accuracy [56] and it works for any shaped boundary as long as it is convex, making it applicable to more complex problems using only a single formulation [55]. The LC-PML method is based on complex coordinate stretching where each coordinate $\boldsymbol{x}$ within the PML region (Ω_{PML}) is mapped to $\tilde{\boldsymbol{x}}$ with a complex coordinate transformation

$$\tilde{\boldsymbol{x}} = \boldsymbol{x} + \frac{1}{jk} f(\zeta)\hat{n}(\zeta) \tag{27}$$

where $k = \omega\sqrt{\epsilon\mu}$. A visualization of the LC-PML is shown in Fig. 3, which shows the associated variables for an arbitrary coordinate inside the PML region. The function $\hat{n}(\zeta)$ is the unit vector defined by

$$\hat{n}(\zeta) = (\boldsymbol{x} - \boldsymbol{x}_0)/\zeta \tag{28}$$

where $\boldsymbol{x}_0$ is the coordinate of the closest point on the inner PML boundary (Γ^{PML}) and ζ is the distance between $\boldsymbol{x}_0$ and $\boldsymbol{x}$ defined by $\zeta = \|\boldsymbol{x} - \boldsymbol{x}_0\|$. Because of the convexity of the PML boundary, $\boldsymbol{x}_0$ is uniquely defined. Furthermore, the function $f(\zeta)$ is a monotonically increasing function of ζ, being zero at the inner boundary to prevent numerical reflections. It is given by

$$f(\zeta) = \frac{\nu\zeta^w}{w\,\|\boldsymbol{x}_1 - \boldsymbol{x}_0\|^{w-1}}, \tag{29}$$

where ν is a positive parameter and w is a positive integer that determines the decay rate inside of the PML region. $\boldsymbol{x}_1$ is the position of point P_1, which is the intersection of the outer PML boundary (Γ^o) and a line passing through $\boldsymbol{x}_0$ and $\boldsymbol{x}$.

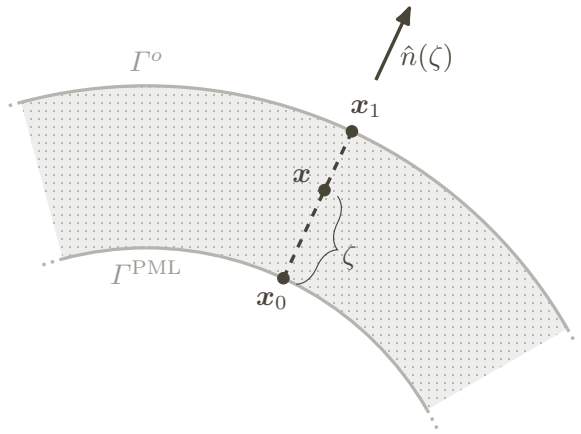

Fig. 3: A visualisation of the implementation of LC-PML. Here, the shaded region is the PML region, $\boldsymbol{x}$ is and arbitrary coordinate inside this region that has its own points $\boldsymbol{x}_0$ and $\boldsymbol{x}_1$ on the inner and outer boundary of the PML region respectively. Furthermore, $\hat{n}(\zeta)$ is the normalized vector from P_0 to P and ζ is the distance between P_0 and P.

2.1.4 Source conditions

Sources from outside of the domain, like plane waves, are often implemented by adding an extra term to the formulation of the ABC which was also briefly discussed in Sec. 2.1.3. But because our domain is surrounded by a PML boundary condition, we cannot implement it this way since the wave would have to travel through the absorbing boundaries. Instead, we use the scattered field formulation, where the total electric field $\boldsymbol{u}$ is decomposed into the *incoming field* $\bar{\boldsymbol{u}}$ (the incident field produced without the scatterer) and the *scattered field* $\boldsymbol{u}^s$ (the resulting field produced by imposing the equivalent current on the surface inside the domain) [55, 57, 58]. The current should, however, not be imposed on Ω_{PML}. Using the scattered field formulation adds another source term to the right hand side of (17)

$$\bar{f} = \left[\frac{\partial}{\partial x}\left(\frac{1}{p}\frac{\partial}{\partial x}\right) + \frac{\partial}{\partial y}\left(\frac{1}{p}\frac{\partial}{\partial y}\right) + q\left(\frac{\omega}{c}\right)^2\right]\bar{u}, \quad \text{for } \boldsymbol{x} \in \Omega \setminus \Omega_{\text{PML}} \tag{30}$$

where $\bar{u}$ is the incident field. The incident field can be arbitrary, but usually is chosen to be a plane wave because the scatterer is away far enough from the source. In the case of a plane wave, the incident fields $\bar{E}_z$ and $\bar{H}_z$ can both be described as

$$\bar{u}(\boldsymbol{x}) = u_0 \exp\left[-jk_0\left(x\cos\bar{\varphi} + y\sin\bar{\varphi}\right)\right], \tag{31}$$

where $k_0 = \omega\sqrt{\epsilon_0\mu_0}$, u_0 is the amplitude and $\bar{\varphi}$ is the incident angle of the plane wave with $\bar{\varphi} = 0$ being along the positive x axis with the positive rotation direction being counter-clockwise. When using an enriched formulation, the enriched degrees of freedom α_i do not correspond directly to the electric or magnetic field at the location of the enriched node. Instead, the original degrees of freedom in support of the enriched node must also be taken into account as shown in (21). The enriched incoming field terms $\bar{\alpha}_i$ are calculated as the difference between the interpolated incoming field from the original mesh nodes and the actual value at the enriched node location, *i.e.*,

$$\bar{\alpha}_i = \frac{1}{s_i \psi_i(\boldsymbol{x}_i)} \left(\bar{u}(\boldsymbol{x}_i) - \sum_{j \in \iota_h} N_j(\boldsymbol{x_i}) \bar{U}_j \right) \tag{32}$$

where $\boldsymbol{x}_i$ is the coordinate of the enriched node, $\psi_i(\boldsymbol{x})$ is the enrichment function associated with enriched node $\boldsymbol{x}_i$, $N_j(\boldsymbol{x})$ and $\bar{\boldsymbol{U}}_j$ are the values of the shape functions and corresponding degrees of freedom of the original nodes with index set ι_h. To regain the total field, the computed scattered field and incoming field can be added together. The addition of the scattered and incoming field inside of the PML region will not create a physical result, so after the addition, the total field is multiplied with a transformation matrix $\boldsymbol{T}$, setting all field values inside of the PML region to zero:

$$\begin{aligned} \boldsymbol{T}\boldsymbol{U}(\boldsymbol{x}) &= \tilde{\boldsymbol{U}}(\boldsymbol{x}), \\ \text{where } \tilde{\boldsymbol{U}}(\boldsymbol{x}) &= 0, \ \forall \boldsymbol{x} \in \Omega_{\text{PML}}. \end{aligned} \tag{33}$$

The matrix $\boldsymbol{T}$ can also be used for applying the source term in (30). The left hand side of (17) can be used for the calculation of the source terms as well, resulting in the system

$$\left(\boldsymbol{M} - \omega^2 \boldsymbol{K}\right) \boldsymbol{U}^s = -\boldsymbol{T} \left[\left(\boldsymbol{M} - \omega^2 \boldsymbol{K}\right) \bar{\boldsymbol{U}} \right]. \tag{34}$$

2.1.5 Far-field calculation

A common use for electromagnetic scattering problems is to investigate the Radar Cross Section (RCS), which describes the reflections of an incident plane wave by a scatterer. The RCS is defined by

$$\sigma_{2\text{D}} = \lim_{R \to \infty} 2\pi R \frac{\left|u^{\text{f}}\right|^2}{|\bar{u}|^2}, \tag{35}$$

where u^{f} is the scattered far-field and R is the observation radius from the scatterer and should satisfy $R \gg 2D/\lambda_0$, where D is the largest dimension of the scatterer and λ_0 is the wavelength in vacuum [55]. The far-field u^{f} can be calculated by using Huygens surface equivalence principle by surrounding the scatterer with a circular interface Γ^{H} and then calculating and integrating the surface electric and magnetic current densities over this interface. The integration over Γ^{H} is done by computing the sum over the element edges along the interface, as shown in Fig. 4. With these equivalent currents, the electric and magnetic far-field can be calculated with [55]

$$\begin{aligned} u^{\text{f}} =& \sqrt{\frac{k_0}{8\pi R}} e^{j\pi/4} e^{-jk_0 R} \sum_{e \in \iota_f} \left(\hat{n}_e^x \cos\theta + \hat{n}_r^y \sin\theta\right) u_e e^{jk(x_e \cos\theta + y_e \sin\theta)} \Delta\ell_e \\ &+ \frac{1}{j\omega} \sqrt{\frac{k_0}{8\epsilon_0\mu_0\pi R}} e^{-j3\pi/4} e^{-jk_0 R} \sum_{e \in \iota_f} \left(\hat{n}_e^x \frac{\partial}{\partial x} + \hat{n}_e^y \frac{\partial}{\partial y} \right) u_e e^{jk(x_e \cos\theta + y_e \sin\theta)} \Delta\ell_e, \end{aligned} \tag{36}$$

where ι_f are the set of element edges along Γ^H, $\hat{n}_e$ is the outward facing normal vector of the eth element edge, θ is the observation angle, u_e, x_e and y_e are the total field strength and coordinates evaluated at the midpoint of the eth element edge respectively, $\Delta\ell^e$ is the length of the element edge. For TM polarization $u = E_z$ and for TE polarization $u = H_z$. Note that when using IGFEM, Γ^H can be created by using a separate enriched interface and thus the discretization can still happen without any prior knowledge about the geometry inside the domain.

2.2 Optimization

The topology optimization methodology in this work combines a level set function to describe the topology with the IGFEM-based analysis procedure described in the previous sections for the analysis. The procedure of defining the material interfaces is the same as described in Sec. 2.1. When using finer meshes, having a design variable on every node of the mesh will allow for very thin and complex

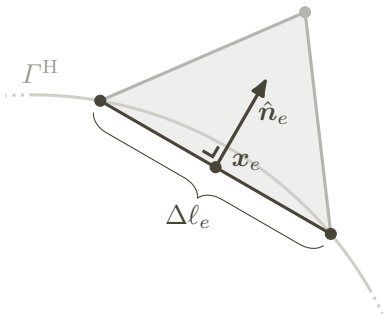

Fig. 4: A schematic showing the eth element with its edge along Γ^{H} and the associated variables

structures that are not realistic. To counter that, compactly supported Radial Basis Functions (RBF) are used [48]

$$\Theta_i\left(r_i\right) = \left(1 - r_i\right)^4 \left(4r_i + 1\right), \quad \text{where} \quad r_i\left(\boldsymbol{x}, \boldsymbol{x}_i\right) = \frac{\sqrt{\|\boldsymbol{x} - \boldsymbol{x}_i\|}}{r_{\mathrm{s}}}, \tag{37}$$

where r_s is the radius of support. Using RBFs the level set function can be interpolated as

$$\phi(\boldsymbol{x}) = \sum_{i \in \iota_s} \Theta_i(\boldsymbol{x}) s_i, \tag{38}$$

where ι_s contains the indices of all design variables s_i. RBFs give the design variables on every node a range of influence over other design variables nearby, which acts as a way to make the design less complex—similarly to a density filter in density-based topology optimization. For more details, the reader is referred to van den Boom et al. [48].

2.2.1 Objective and sensitivities

As an example, we implement a figure of merit to focus light onto a chosen point, subject to an incoming plane wave. This figure of merit has been taken from Christiansen and Sigmund [52], where they use a density-based topology optimization approach. It can be formulated as the weighted sum of light intensity $|E_z|^2$ at chosen nodes in the mesh. The general optimization problem can then be written as

$$\begin{aligned} \min_{\boldsymbol{d}} \quad & \Psi = -\boldsymbol{E}_z^{\mathrm{H}} \boldsymbol{P} \boldsymbol{E}_z \\ \text{subject to} \quad & \left(\boldsymbol{M}(d) - \omega^2 \boldsymbol{K}(d)\right) \boldsymbol{E}_z^{\mathrm{s}} = -\left(\boldsymbol{M}(d) - \omega^2 \boldsymbol{K}(d)\right) \bar{\boldsymbol{E}}_z, \\ & d_{\min} \leq d \leq d_{\max} \end{aligned} \tag{39}$$

with $\boldsymbol{P}$ being a diagonal matrix which selects and weight the points at which to maximize the light intensity, $\bullet^{\mathrm{H}}$ is the conjugate transpose and $d_{\min}$ and $d_{\max}$ are the lower and upper bounds of the design variables d, which are used to prevent the level set function from becoming too steep. The optimization problem is solved using the Method of Moving Asymptotes (MMA) [59], which also requires the sensitivities of the objective with respect to the design variables. These can be calculated with

$$\frac{\partial \Psi}{\partial s_i} = \frac{\partial \Psi}{\partial E_{z,k}} \frac{\partial E_{z,k}}{\partial \phi_j} \frac{\partial \phi_j}{\partial d_i}. \tag{40}$$

The first term on the right-hand side of (40) is the derivative of the objective function with respect to the electric field values

$$\frac{\partial \Psi}{\partial E_{z,k}} = -2 E_{z,m}^* P_{mk}, \tag{41}$$

where $\bullet^*$ is the complex conjugate. The second term is the derivative of the electric field, with respect to every level set value, which can be calculated by solving the linear equation

$$\left(\boldsymbol{M} - \omega^2 \boldsymbol{K}\right) \frac{\partial E_{z,k}^s}{\partial \phi_j} = \left(\frac{\partial \boldsymbol{M}}{\partial \phi_j} - \omega^2 \frac{\partial \boldsymbol{K}}{\partial \phi_j}\right) E_{z,k}^s - \boldsymbol{T} \left[\left(\frac{\partial \boldsymbol{M}}{\partial \phi_j} - \omega^2 \frac{\partial \boldsymbol{K}}{\partial \phi_j}\right) \bar{E}_{z,k} + \left(\boldsymbol{M} - \omega^2 \boldsymbol{K}\right) \frac{\partial \bar{E}_{z,k}}{\partial \phi_j}\right]. \tag{42}$$

to find the derivative of the scattered field, after which the derivative of the incoming field can be added to get the the total field derivative with respect to every level set value. For a more detailed explanation of the sensitivities see Appendix A, which also contains a verification of the analytical sensitivities using a finite difference scheme. Because this equations has the same left-hand side as (34), factorization of the system matrix, for example an LU decomposition, can be reused for efficiency.

Finally, the third term is the derivative of the nodal level set values with respect to the design variables, which is defined as

$$\frac{\partial \boldsymbol{\phi}}{\partial \boldsymbol{d}} = \boldsymbol{\Theta}^{\mathrm{T}}, \tag{43}$$

where $\boldsymbol{\Theta}$ is the matrix defined in (37).

2.3 Results

In this section, three example problems will be presented. First, an eigenvalue analysis will be performed to find the band structures of photonic crystal designs from the literature. Then, a Mie scattering problem is solved and a convergence analysis is done for both the standard finite element method (h-FEM) and IGFEM, to check the implementation of the source conditions and absorbing boundary conditions. Finally, an optimization taken from the literature of a 2D metalens and reflector is done to test the implementation of the level set-based optimization using IGFEM.

2.3.1 Band structure analysis

First, a band gap analysis is performed on a photonic crystal unit cells with a circular inclusion, taken from Joannopoulos et al. [11], using both h-FEM and IGFEM [11]. A illustration of the problem is shown in Fig. 5, where b is the radius of the circular inclusion, β is the angle between the lattice vectors $\boldsymbol{a}_1$ and $\boldsymbol{a}_2$, Ω_1 and Ω_2 are domains with relative permittivity ϵ_{r1} and ϵ_{r2} respectively, and Γ^{B1} and Γ^{B2} are the Bloch-Floquet boundary conditions. In all examples $\|\boldsymbol{a}_1\| = \|\boldsymbol{a}_2\| = a$, where a is also known as the lattice constant. As discussed earlier, in order to compute the complete band structure of a photonic crystal, an eigenvalue analysis must be done for all wave vectors $\boldsymbol{k}$. However, because of the translational and rotational symmetry of the photonic crystal lattice, the wave vectors that need to be considered can be reduced significantly. This collection of wave vectors is called the irreducible brillioun zone.

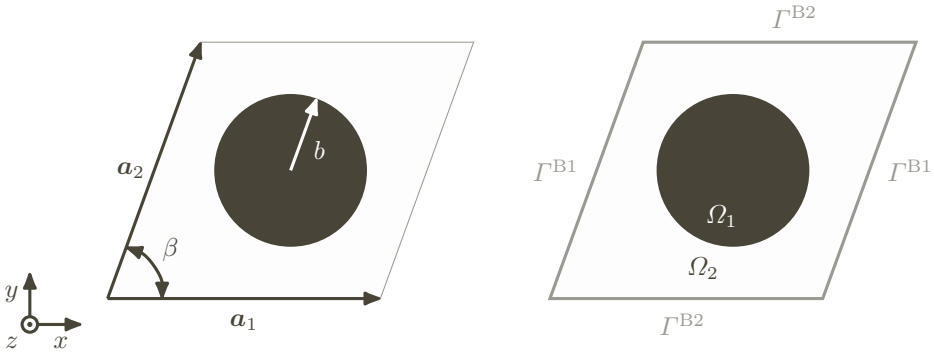

Fig. 5: On the left: an illustration of a photonic crystal unit cell for an arbitrary lattice with angle β and a circular inclusion with radius b. On the right: the computational domain and boundary conditions used for the simulation.

As a first example, we perform the band structure analysis of a square lattice with $b = 0.2a$, $\beta = 90°$, $\epsilon_{r1} = 8.9$ and $\epsilon_{r2} = 1$. Fig. 6 shows the unit cell with the corresponding (irreducible) brillioun zone on the left, together with the computed band structure for both TM and TE modes, using either h-FEM or IGFEM with a mesh size of $\Delta h = 3a/100$, on the right. It can be seen that the band structure results obtained using h-FEM and IGFEM are very similar.

As a second example, we perform the band structure analysis of a hexagonal lattice with $b = 0.48a$, $\beta = 60°$, $\epsilon_{r1} = 1$ and $\epsilon_{r2} = 13$. Fig. 7 shows the unit cell with the corresponding (irreducible) brillioun zone on the left, together with the computed band structure for both TM and TE modes, using either h-FEM or IGFEM with a mesh size of $\Delta h = 3a/100$, on the right. Again there is almost no difference between the result obtained using h-FEM and IGFEM. Comparing all band structure results to the band structures shown in Joannopoulos et al. [11], it can be noted that they are very similar as well [11].

2.3.2 Mie scattering problem

Next, we verify the implementation of the electromagnetic scattering problem in 2D using both h-FEM and IGFEM. This can be done using Mie scattering, which describes the scattering of a electromagnetic plane wave with a cylinder. The dielectric cylinder has a radius m with relative permittivity $\epsilon_r = 2$

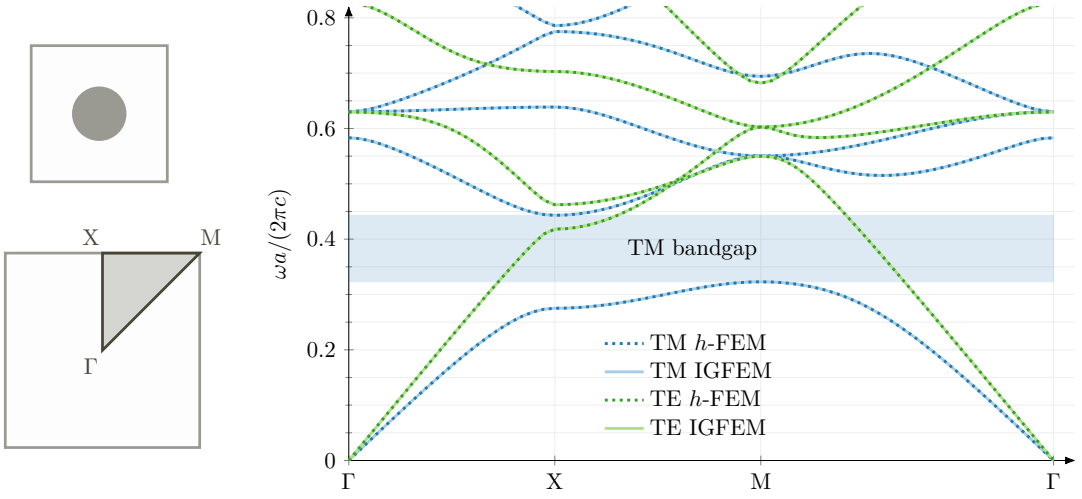

Fig. 6: On the left: an illustration of the square periodic unit cell with its corresponding (irreducible) brillioun zone. On the right: the obtained TM and TE band structure using both h-FEM and IGFEM.

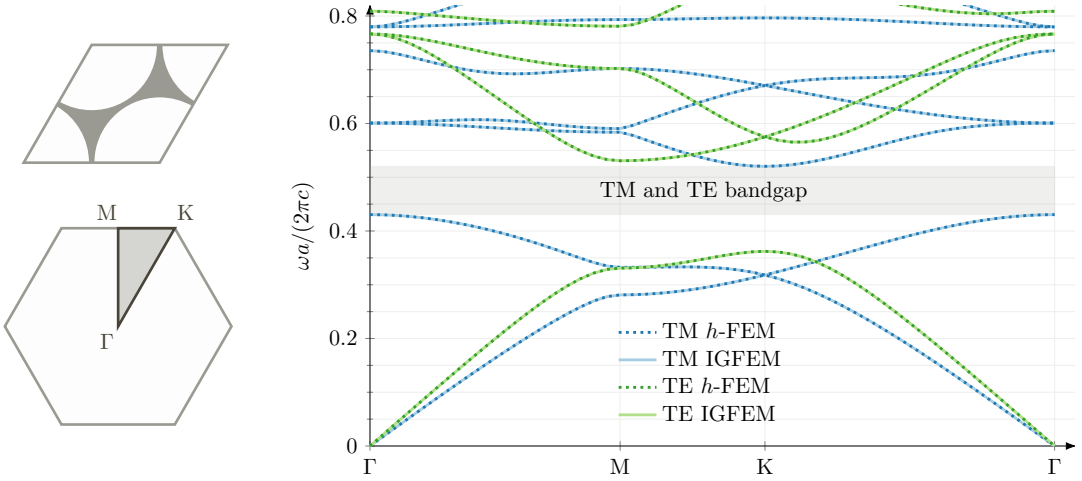

Fig. 7: On the left: an illustration of the hexagonal periodic unit cell with its corresponding (irreducible) brillioun zone. On the right: the obtained TM and TE band structure using both h-FEM and IGFEM.

surrounded by vacuum ($\epsilon_r = 1$) layer with thickness $t_\mathrm{v} = 0.4m$. A PML layer with thickness $t_\mathrm{PML} = 0.7m$ is placed at the edges of the domain to absorb outgoing waves. An illustration is shown in Fig. 8 where Ω_d is the dielectric, Ω_v is the surrounding background medium, Ω_PML is the PML region, Γ^N is the homogeneous Neumann boundary condition for symmetry and Γ^H is the Huygens surface. We introduce a plane wave with wavelength $\lambda = m$ and angle of incidence $\bar{\varphi} = \pi/2$ (towards the positive y direction). The solutions to Mie scattering problems can also be calculated with analytical equations. Using wave transformation, a plane wave with unity magnitude and angle of incidence $\bar{\varphi}$ can be expressed in terms of cylindrical waves

$$\exp\left[-jk_0\left(x\cos\bar{\varphi} + y\sin\bar{\varphi}\right)\right] = \sum_{n=-\infty}^{\infty} j^{-n} J_n(k_0\rho) e^{jn(\varphi-\bar{\varphi})}, \tag{44}$$

where J_n is the nth order Bessel function of the first kind and ρ and φ are the radial coordinate and the azimuth. Using this assumption, the scattering of a plane wave by a dielectric cylinder can be calculated with

$$u^\mathrm{s} = \begin{cases} \sum_{n=-\infty}^{\infty} a_n H_n^{(2)}(k_0\rho) e^{jn(\varphi-\bar{\varphi})} & \text{for} \quad \rho \geq m \\ \sum_{n=-\infty}^{\infty} b_n J_n(k\rho) e^{jn(\varphi-\bar{\varphi})} - j^{-n} J_n(k_0\rho) e^{jn(\varphi-\bar{\varphi})} & \text{for} \quad \rho < m \end{cases} \tag{45}$$

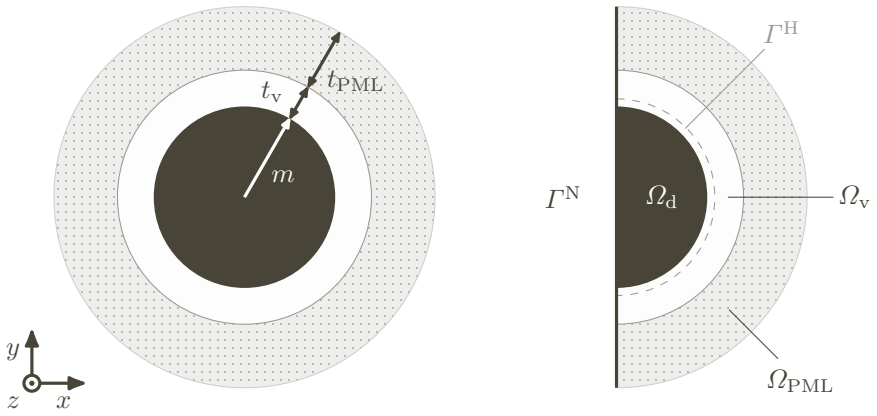

Fig. 8: On the left: an illustration of the Mie scattering problem with dimensions. On the right: the computational domain and boundary conditions used for the simulation.

where the terms a_n and b_n are given by

$$a_n = -j^{-n} \frac{\sqrt{p} J_n'(k_0 m) J_n(km) - \sqrt{q} J_n(k_0 m) J_n'(km)}{\sqrt{p} H_n^{(2)\prime}(k_0 m) J_n(km) - \sqrt{q} H_n^{(2)}(k_0 m) J_n'(km)} \tag{46}$$

$$b_n = \frac{j^{-(n+1)}}{\pi k_0 m} \frac{2\sqrt{p}}{\sqrt{p} H_n^{(2)\prime}(k_0 m) J_n(km) - \sqrt{q} H_n^{(2)}(k_0 m) J_n'(km)}. \tag{47}$$

where, for a TM polarized plane wave $u^{\mathrm{s}} = E_z^{\mathrm{s}}$, $p = \mu_r$ and $q = \epsilon_r$, while for a TE polarized plane wave $u^{\mathrm{s}} = H_z^{\mathrm{s}}$, $p = \epsilon_r$ and $q = \mu_r$ [57, 60]. J_n' is the derivative of the nth order Bessel function of the first kind, $H_n^{(2)}$ and $H_n^{(2)\prime}$ are the nth order Hankel function of the second kind and its derivative respectively. Note that these equations are an approximation as the scattered field is a superposition of the terms in the summation in (45) [57], where increasing the amount of terms will yield a better result. In this thesis we choose $n \in [-100 \dots 100]$.

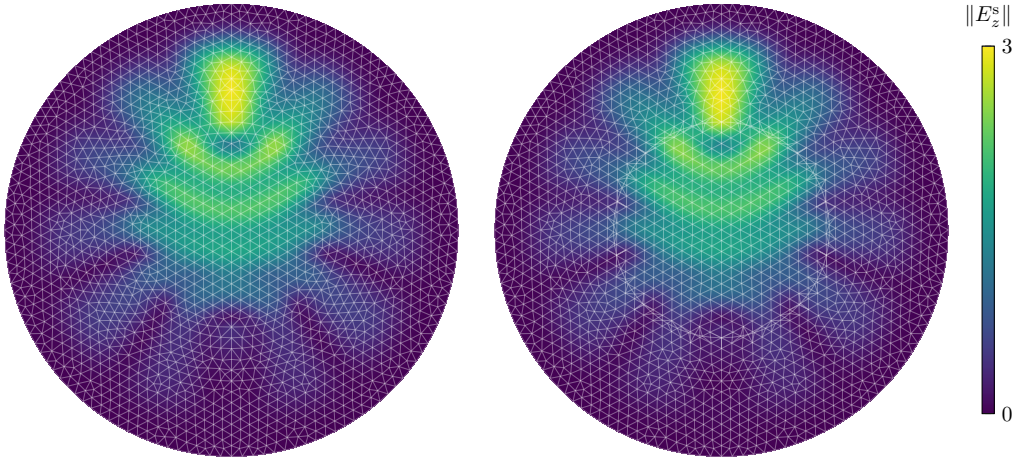

Fig. 9: The electric field norm of the scattered field for TM polarization obtained using h-FEM (on the left) and using IGFEM (on the right).

First, we consider the Mie scattering problem for a TM polarized plane wave. The problem is solved using h-FEM together with a mesh which is conforming to the geometry. The same problem is solved with a mesh which is nonconforming to the geometry, using IGFEM to resolve the field in the elements cut by the dielectric inclusion. Fig. 9 shows the scattered field for both methods with a mesh size of $\Delta h = \lambda/10$. Fig. 10 shows the result of the Mie scattering problem for a TE polarized plane wave. Using the exact solution presented (45) we study the element-wise error with respect to the analytical solution, which is given by

$$||e||_{\mathcal{L}^2} = \frac{||\boldsymbol{u} - \boldsymbol{u}^h||}{||\boldsymbol{u}||} = \frac{\int_e (\boldsymbol{u} - \boldsymbol{u}^h)^{\mathrm{H}} (\boldsymbol{u} - \boldsymbol{u}^h) \mathrm{d}e}{\int_e ||\boldsymbol{u}||^2 \mathrm{d}e}. \tag{48}$$

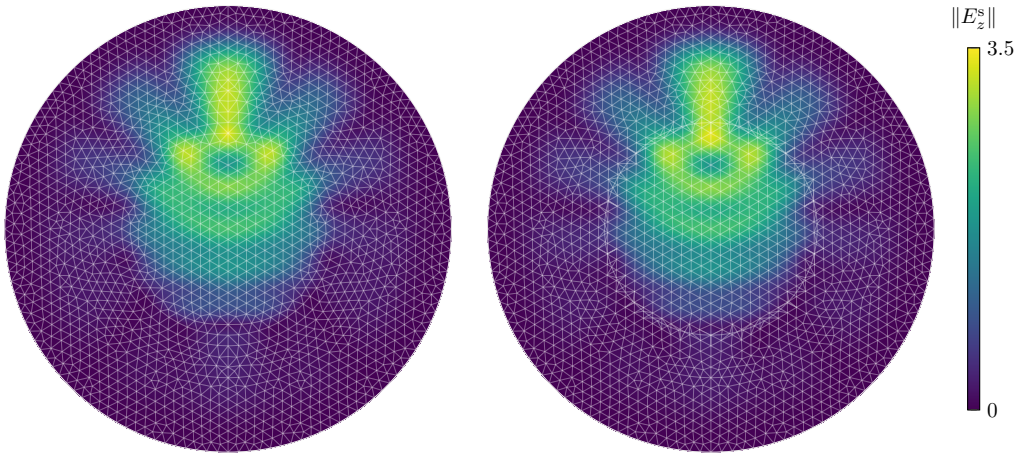

Fig. 10: The electric field norm of the scattered field for TE polarization obtained using h-FEM (on the left) and using IGFEM (on the right).

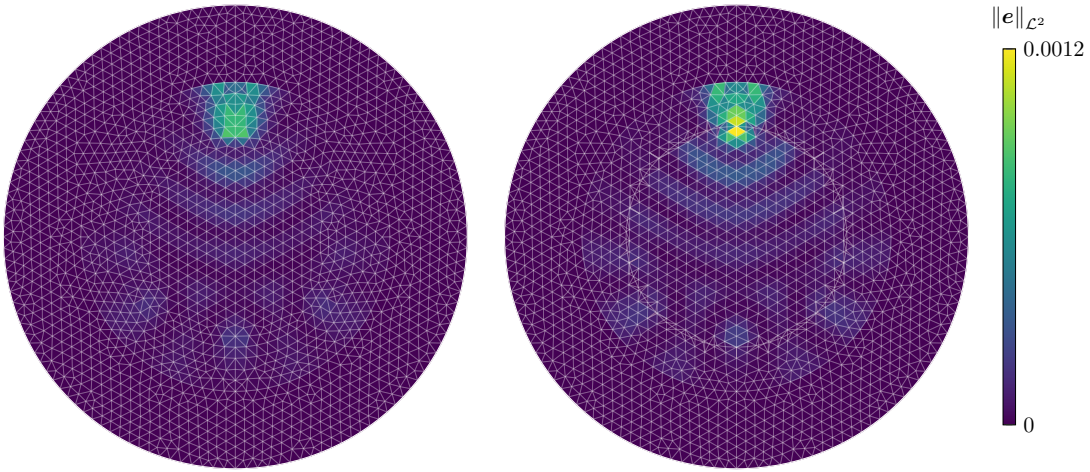

Fig. 11: The $\mathcal{L}^2$-norm of the element-wise error for TM polarization obtained using h-FEM (on the left) and using IGFEM (on the right).

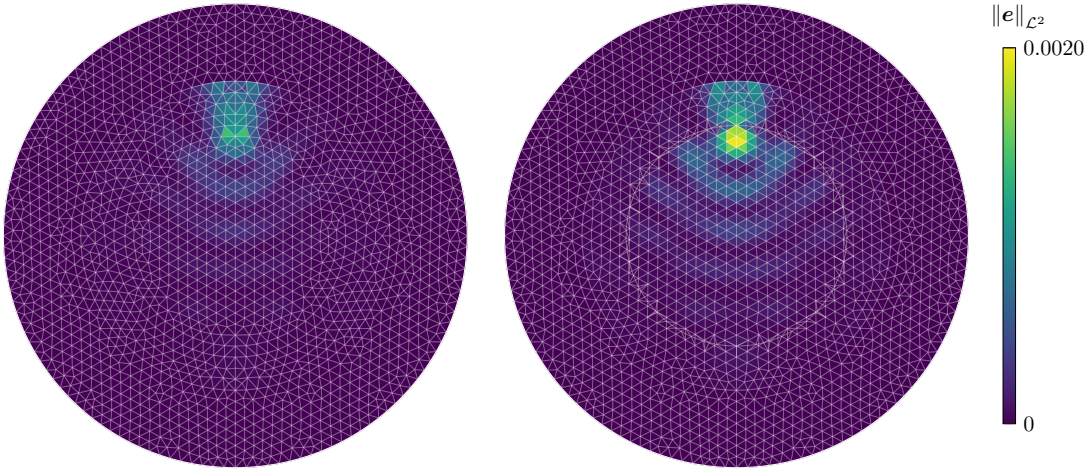

Fig. 12: The $\mathcal{L}^2$-norm of the element-wise error for TE polarization obtained using h-FEM (on the left) and using IGFEM (on the right).

Fig. 11 and Fig. 12 show the element-wise error in the scattered field for TM and TE polarization, respectively. The error in the PML region is not taken into account since the solution in that region is considered nonphysical.

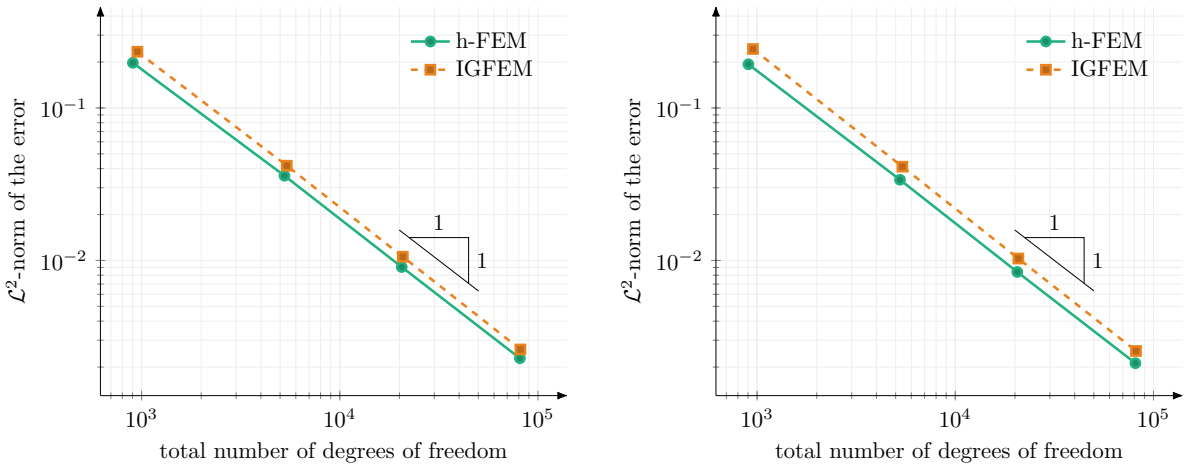

Fig. 13: On the left: The convergence of the $\mathcal{L}^2$-norm of the error for the TM polarization case. On the right: The convergence of the $\mathcal{L}^2$-norm of the error for the TE polarization case.

Next, a convergence analysis is done using both h-FEM and IGFEM, where the $\mathcal{L}^2$-norm of the error is accumulated over all elements for increasing mesh sizes $\Delta h = \lambda/10$, $\lambda/10$, $\lambda/25$, $\lambda/50$ and $\lambda/100$. The global measure of error in the $\mathcal{L}^2$-norm using h-FEM and IGFEM is plotted against the total number of degrees of freedom for both the TM and TE polarization cases in Fig. 13. In all cases, the convergence rate is equal to a slope of -1, which is the optimal rate for the $\mathcal{L}^2$-norm. This means that the optimal convergence of h-FEM is recovered using the IGFEM method for electromagnetic problems. Note that despite the optimal convergence rate, the accuracy of IGFEM is slightly lower than h-FEM.

Finally, the RCS is calculated with $R = 100\,\mathrm{m}$ using the Huygens surface equivalence principle for increasing mesh sizes $\Delta h = \lambda/10$, $\lambda/10$, $\lambda/25$, $\lambda/50$ and $\lambda/100$. The analytical solution presented in (45) can also be used for verifying the RCS results. Fig. 14 and Fig. 15 show the RCS obtained with both h-FEM and IGFEM for TM and TE polarizations, respectively. It can be seen that as the mesh size decreases, the computed RCS gets closer to the analytically calculated RCS.

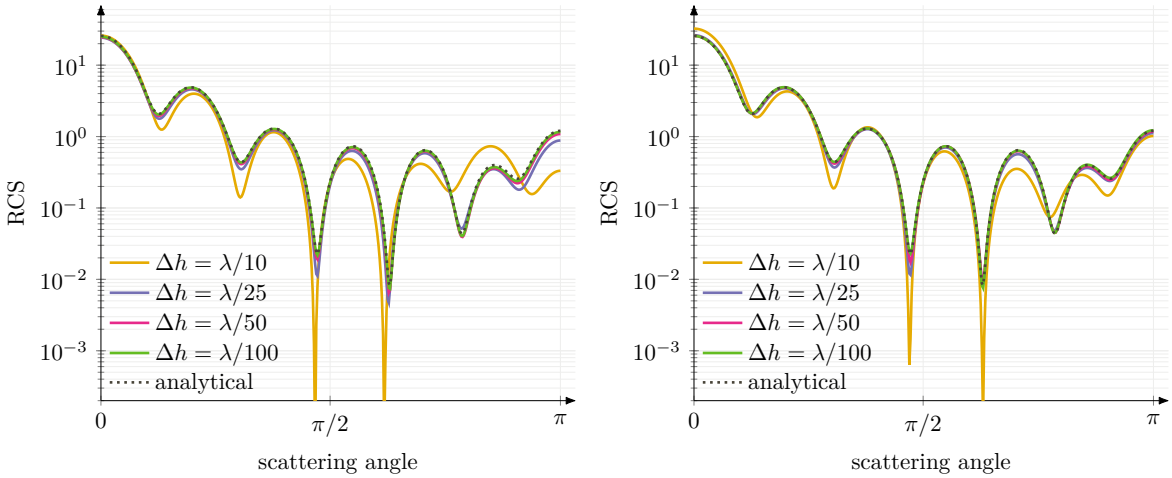

Fig. 14: The analytical and numerical RCS for TM polarization with decreasing mesh sizes obtained using h-FEM (on the left) and using IGFEM (on the right)

2.3.3 Optimizing for energy concentration

Now that the IGFEM-based analysis has been verified, we consider the optimization problem studied by Christiansen and Sigmund [52], where the performances of both a 2D meta-lens and a reflector subject to an incoming plane wave, are maximized. An illustration of the problem and the computational

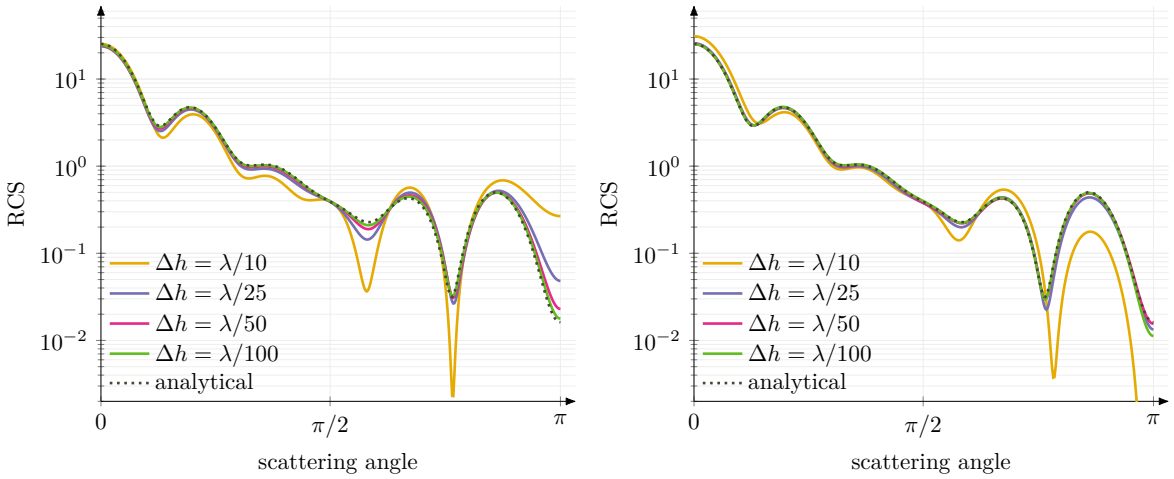

Fig. 15: The analytical and numerical RCS for TE polarization with decreasing mesh sizes obtained using h-FEM (on the left) and using IGFEM (on the right)

domain for both optimization problems is shown in Fig. 16. We choose the height of the domain as h and width as $w = 2h$. The height of the dielectric substrate Ω_d is $h_\mathrm{d} = 0.1h$, the height of the design area Ω_des is $h_\mathrm{des} = 0.075h$, and the thickness of the PML layer surrounding the domain Ω_PML is $t_\mathrm{PML} = 0.175h$. r_f is the chosen focal point of the lens/reflector, Ω_v is the surrounding background medium, and Γ^N is the homogeneous Neumann boundary condition for symmetry. The two initial designs used in both optimization problems are shown in Fig. 17, where the designs on the top and bottom will be referred to as the first and second initial design, respectively.

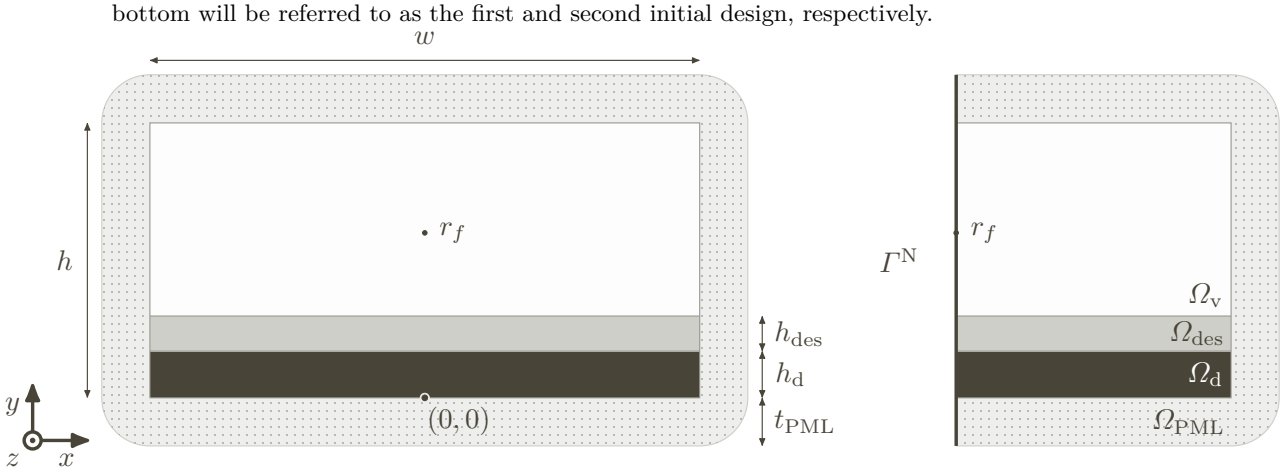

Fig. 16: On the left: an illustration of the optimization problem with dimensions. On the right: the computational domain and boundary conditions used for the simulation.

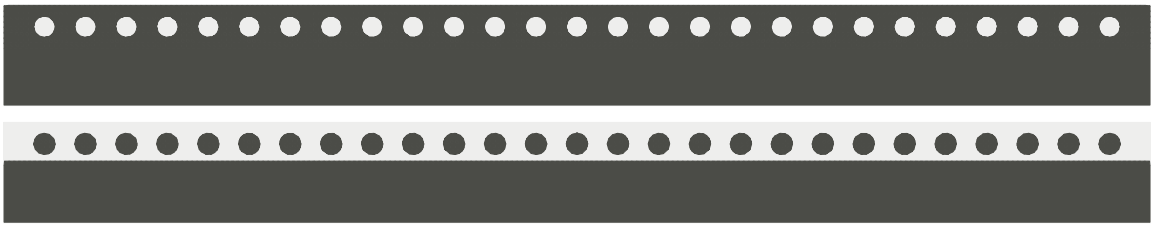

Fig. 17: The first and second initial design used for both the metalens and reflector optimization

First, we maximize the light intensity $|E_z|^2$ for a metalens at the focal point r_f with coordinate $\boldsymbol{x}_f = (0, 0.6h)$. We introduce a plane wave with wavelength $\lambda = 0.175h$ and an angle of incidence $\bar{\varphi} = \pi/2$ (towards the positive y direction). The dielectric material has a relative permittivity of $\epsilon_r = 2$ and is surrounded by vacuum (ϵ_r=1). The mesh size is equal to $\Delta h = \lambda/(10\epsilon_r)$ everywhere except for the design area Ω_des where it is equal to $\Delta h = \lambda/20$.

Secondly, we maximize the light intensity $\left|E_z^2\right|$ for a reflector at the focal point r_f with coordinate $\boldsymbol{x}_f = (0, 0.5h)$. We introduce a plane wave with wavelength $\lambda = 0.175h$ and angle of incidence

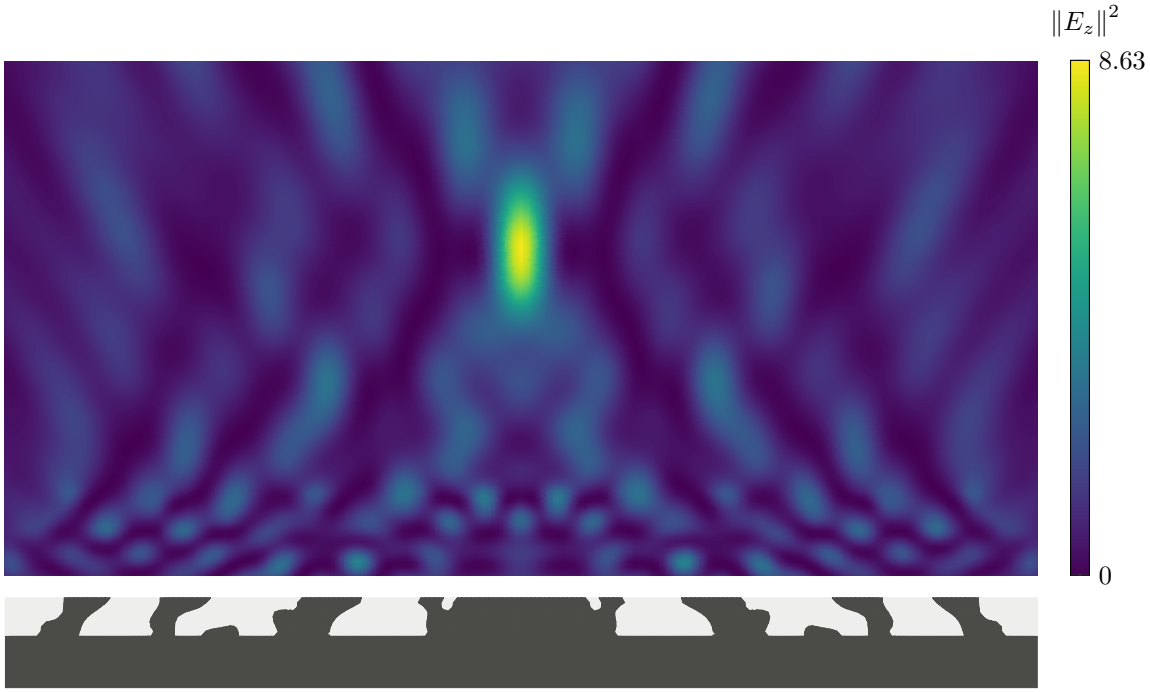

Fig. 18: The optimized metalens design starting from the first initial design together with the resulting electric field intensity

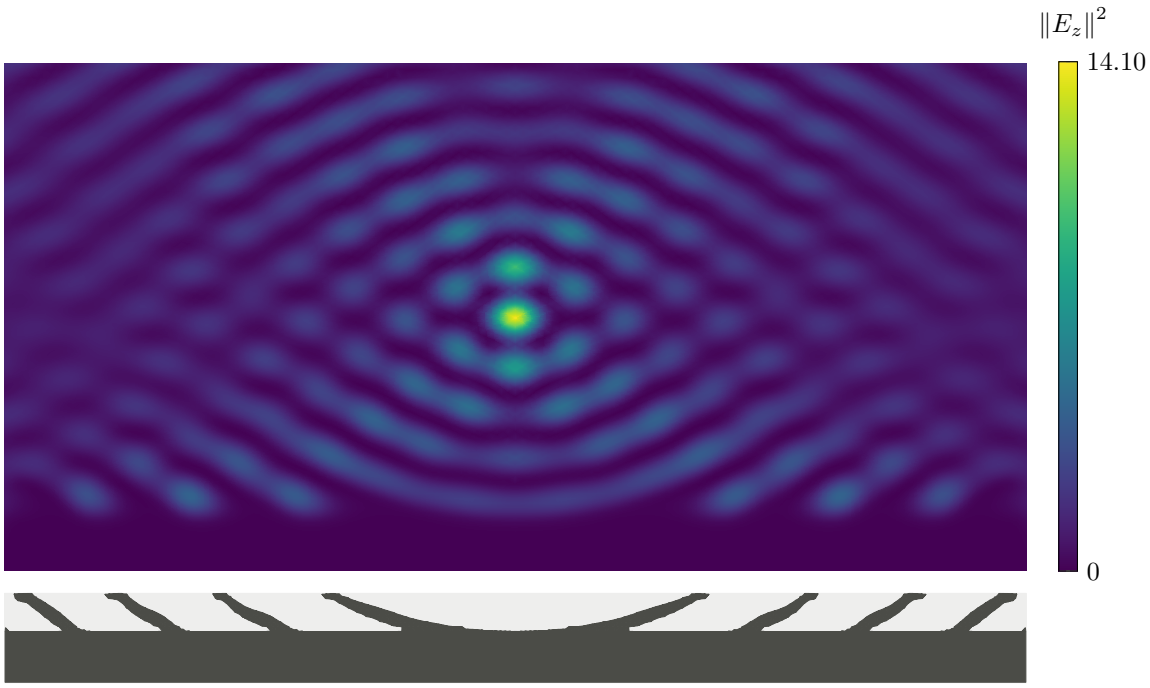

Fig. 19: The optimized metalens design starting from the second initial design together with the resulting electric field intensity.

$\bar{\varphi} = -\pi/2$ (towards the negative y-direction). The dielectric material has a relative permittivity of $\epsilon_r = 1.36 - 6.08j$ and is surrounded by vacuum ($\epsilon_r = 1$). The mesh size is equal to $\Delta h = \lambda/(10\epsilon_r)$ everywhere except for the design area Ω_{des} where it is equal to $\Delta h = \lambda/20$.

Fig. 18 shows the optimized metalens design and resulting electric field intensity. Both initial designs resulted in very similar optimized design and performance, as can be seen in Fig. 20 on the left. However, the fact that the optimized performance and designs are not exactly the same for

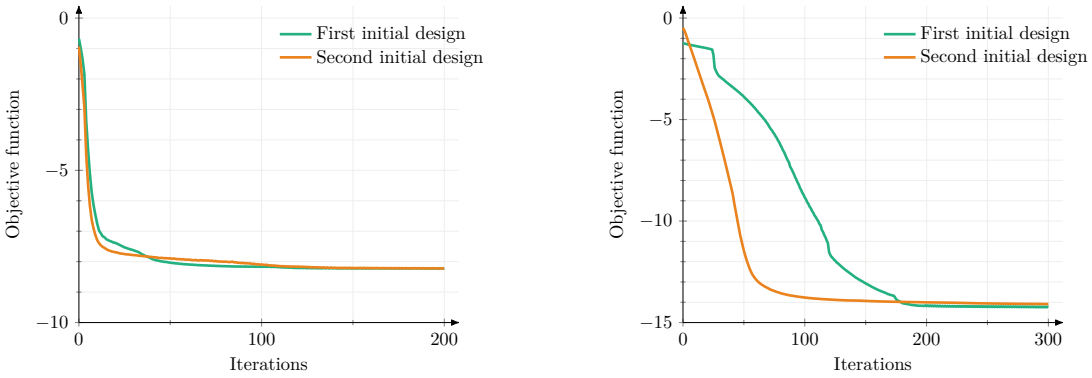

Fig. 20: On the left: the convergence of the metalens objective function for both initial designs. On the right: the convergence of the reflector objective function for both initial designs

the two initial design indicates that this is non-convex optimization. The same optimization problem was solved using a density-based optimization approach taken from Christiansen and Sigmund [52], using various filter radii. The maximum light intensity obtained is ≈ 7.2, whereas the maximum field strength using our method is ≈ 8.2.

Fig. 19 shows the optimized reflector design and the resulting electric field intensity. The first initial design resulted in a slightly better performance, but since the optimized design contained non-feasible geometry (in the form of floating material) the second initial design was chosen as the best result. Just like the metalens optimization, the results of the reflector optimization indicate that this is non-convex optimization. Again, the same optimization problem was solved using a density-based optimization approach taken from Christiansen and Sigmund [52], using various filter radii. The maximum light intensity obtained is ≈ 12.1, whereas the maximum field strength using our method is ≈ 14.1.

2.4 Summary and conclusion

First, we presented a 2D IGFEM-based analysis for electromagnetic problems. This method allows for the simulation of different geometries without the need to generate a geometry conforming mesh.

Secondly, a band structure analysis was performed on photonic crystal designs taken from Joannopoulos et al. [11] using h-FEM and IGFEM, both showing similar results to the literature [11]. On top of that, a convergence analysis was done on a Mie scattering problem for both TM and TE polarization cases, which showed that IGFEM recovered the optimal convergence of h-FEM. Moreover, a far-field analysis was done, which also showed correct results for both h-FEM and IGFEM.

Finally, a 2D IGFEM-based level set optimization method was presented, which can be used as an alternative to density based optimization methods commonly found in the literature. An optimization was performed where the ability of a 2D meta-lens and a 2D reflector to focus light onto a chosen point, was maximized. The results of both methods showed similarities with the designs found in the literature, which implies that the IGFEM-based level set optimization is well suited for optimizing photonic devices. It can be seen that for both optimization problems the results obtained using the level set optimization combined with the IGFEM analysis are slightly better than the results obtained using density-based optimization taken from the literature.

In conclusion, this work presents the first level set topology optimization for electromagnetic problems using IGFEM. Moreover, it shows the flexibility of IGFEM for simulating electromagnetic problems without the need of geometry conforming meshes, which is especially useful for optimization problems. Finally, from the optimization examples we can conclude that the proper interface representation throughout the optimization of IGFEM can help with convergence to better optimized designs for some optimization problems.

3

Reflection

The planning for this project at the point of handing in my literature review was very different to the actual result. I did not manage to implement the nanocavity optimization from Wang et al. [22], because for this optimization problem a 3D simulation was needed which would have taken a lot more time to implement. Instead it was changed to a more simple optimization which can be done with a 2D simulation and is still pretty close (in my opinion) to the original goal. Also, I did not manage to make the optimization robust to spatial variations, which was also planned at the start. This, because my project had already been going on for very long at the point I finally got the optimization working, at which point ending the project on a different optimization problem was the best option. The formulation also changed, using the scattered field formulation with PML instead of using absorbing boundary conditions.

Probably the most important point I noticed for me to improve upon is communication. When there were no results to be shown or if I was stuck on a problem, I often did not reach out in time. Doing so often resulted in getting stuck on problems for longer and getting less motivated for the project. Towards the end of the project I tried to improve my communication, but I know that it is still something that needs further improvement.

The overall planning of this project was also not that great. I barely took any extra time into account for the time that is going to be lost if I get stuck on anything and/or something does not work. Also I did not have a plan B for every step in my project, *e.g.*, a plan B for if I failed to make the simulation formulation work and a plan C for if I failed to make the cavity and the band gap optimization work. Spending time on these failed attempts and needing to find an alternative cost a lot of time. Also it did take some time to learn the code in Hybrida. Knowing how the code works is of course necessary to make additions to it, but also for debugging. Sometimes the use of complex numbers within the implementation of electromagnetics caused some issues that were difficult to predict as these often did not give an error message to locate the issue. Set-backs and problems will always happen in a project and I should have taken that into account more by making back-up plans for all of the steps or allocate more time for every step.

Although 2D simulation can approximate in-plane devices with in-plane light propagation, 3D simulation allows for the simulation of many different photonic applications. For future implementation, it would thus be useful to extend the code to 3D. However, this would be quite challenging as it would either need a different formulation when using nodal elements or the implementation of (enriched) edge elements. After that, the implementation of new figure of merits for optimization would be easier in comparison as the framework of the 2D optimization could be reused for the most part.

Overall, doing this research project has definitely been a learning experience for me. Even though I did not achieve my original goal and took more time for my project than intended, I think the final result of this project is still good. Lastly, I want to thank Dr. Richard A. Norte and Dr. Alejandro M. Aragón and both their groups for their kindness, patience, and help towards me during this project.

References

[1] S. Molesky, Z. Lin, A. Y. Piggott, W. Jin, J. Vučković, and A. W. Rodriguez. Inverse design in nanophotonics. *Nature Photonics*, 12(11):659–670, 11 2018. ISSN 1749-4885. doi: 10.1038/s41566-018-0246-9. URL http://www.nature.com/articles/s41566-018-0246-9.

[2] A. F. Koenderink, A. Alù, and A. Polman. Nanophotonics: Shrinking light-based technology. *Science*, 348(6234):516–521, 5 2015. ISSN 0036-8075. doi: 10.1126/science.1261243. URL https://www.science.org/doi/10.1126/science.1261243.

[3] Baohua Jia. Nanophotonics silicon solar cells: status and future challenges. *Nanotechnology Reviews*, 4(4):337–346, 1 2015. ISSN 2191-9097. doi: 10.1515/ntrev-2015-0025. URL https://www.degruyter.com/document/doi/10.1515/ntrev-2015-0025/html.

[4] O. Painter, R. K. Lee, A. Scherer, A. Yariv, J. D. O'Brien, P. D. Dapkus, and I. Kim. Two-Dimensional Photonic Band-Gap Defect Mode Laser. *Science*, 284(5421):1819–1821, 6 1999. ISSN 0036-8075. doi: 10.1126/science.284.5421.1819. URL https://www.science.org/doi/10.1126/science.284.5421.1819.

[5] W. R. Frei, H. T. Johnson, and K. D. Choquette. Optimization of a single defect photonic crystal laser cavity. *Journal of Applied Physics*, 103(3):1–7, 2008. doi: 10.1063/1.2838173. URL https://doi.org/10.1063/1.2838173.

[6] A. Harhouz and A. Hocini. Design of high-sensitive biosensor based on cavity-waveguides coupling in 2D photonic crystal. *Journal of Electromagnetic Waves and Applications*, 29(5):659–667, 2015. ISSN 15693937. doi: 10.1080/09205071.2015.1012597. URL http://dx.doi.org/10.1080/09205071.2015.1012597.

[7] G. Pitruzzello and T. F. Krauss. Photonic crystal resonances for sensing and imaging. *Journal of Optics*, 20(7):1–23, 2018. ISSN 2040-8978. doi: 10.1088/2040-8986/aac75b. URL https://iopscience.iop.org/article/10.1088/2040-8986/aac75b.

[8] H. Altug, S. Oh, S. A. Maier, and J. Homola. Advances and applications of nanophotonic biosensors. *Nature Nanotechnology*, 17(1):5–16, 2022. ISSN 1748-3395. doi: 10.1038/s41565-021-01045-5. URL https://doi.org/10.1038/s41565-021-01045-5.

[9] J. N. Anker, W. P. Hall, O. Lyandres, N. C. Shah, J. Zhao, and R. P. Van Duyne. Biosensing with plasmonic nanosensors. *Nature Materials*, 7(6):442–453, 2008. ISSN 1476-4660. doi: 10.1038/nmat2162. URL https://doi.org/10.1038/nmat2162.

[10] G. Ruiz-Vega, M. Soler, and L. M. Lechuga. Nanophotonic biosensors for point-of-care {COVID}-19 diagnostics and coronavirus surveillance. *Journal of Physics: Photonics*, 3(1):11002, 2021. doi: 10.1088/2515-7647/abd4ee. URL https://doi.org/10.1088/2515-7647/abd4ee.

[11] J. D. Joannopoulos, S. G. Johnson, J. N. Winn, and R. D. Meade. *Photonic Crystals Molding the Flow of Light*. Princeton University Press, Princeton and Oxford, 2nd editio edition, 2007. URL http://ab-initio.mit.edu/book/.

[12] K. Ashida, M. Okano, M. Ohtsuka, M. Seki, N. Yokoyama, K. Koshino, M. Mori, T. Asano, S. Noda, and Y. Takahashi. Ultrahigh-Q photonic crystal nanocavities fabricated by CMOS process technologies. *Optics Express*, 25(15):18165, 7 2017. ISSN 1094-4087. doi: 10.1364/OE.25.018165. URL https://opg.optica.org/abstract.cfm?URI=oe-25-15-18165.

[13] T. Asano, B. S. Song, Y. Akahane, and S. Noda. Ultrahigh-Q Nanocavities in Two-Dimensional Photonic Crystal Slabs. *IEEE Journal of Selected Topics in Quantum Electronics*, 12(6):1123–1134, 11 2006. ISSN 1077-260X. doi: 10.1109/JSTQE.2006.881639. URL http://ieeexplore.ieee.org/document/4032626/.

[14] M. Minkov and V. Savona. Automated optimization of photonic crystal slab cavities. *Scientific Reports*, 4(1):5124, 5 2015. ISSN 2045-2322. doi: 10.1038/srep05124. URL http://www.nature.com/articles/srep05124.

[15] Z. Zhang and M. Qiu. Small-volume waveguide-section high Q microcavities in 2D photonic crystal slabs. *Optics Express*, 12(17):3988, 2004. ISSN 1094-4087. doi: 10.1364/OPEX.12.003988. URL https://opg.optica.org/oe/abstract.cfm?uri=oe-12-17-3988.

[16] D. Wang, Z. Yu, Y. Liu, X. Guo, C. Shu, S. Zhou, and J. Zhang. Ultrasmall modal volume and high Q factor optimization of a photonic crystal slab cavity. *Journal of Optics*, 15(12):125102, 12 2013. ISSN 2040-8978. doi: 10.1088/2040-8978/15/12/125102. URL https://iopscience.iop.org/article/10.1088/2040-8978/15/12/125102.

[17] J. S. Jensen and O. Sigmund. Topology optimization for nano-photonics. *Laser & Photonics Reviews*, 5(2):308–321, 3 2011. ISSN 18638880. doi: 10.1002/lpor.201000014. URL https://onlinelibrary.wiley.com/doi/10.1002/lpor.201000014.

[18] J. K. Guest, J. H. Prévost, and T. Belytschko. Achieving minimum length scale in topology optimization using nodal design variables and projection functions. *International Journal for Numerical Methods in Engineering*, 61(2):238–254, 2004. ISSN 00295981. doi: 10.1002/nme.1064.

[19] M. Zhou, B. S. Lazarov, F. Wang, and O. Sigmund. Minimum length scale in topology optimization by geometric constraints. *Computer Methods in Applied Mechanics and Engineering*, 293:266–282, 8 2015. ISSN 00457825. doi: 10.1016/j.cma.2015.05.003. URL https://linkinghub.elsevier.com/retrieve/pii/S0045782515001693.

[20] H. Men, K. Y. K. Lee, R. M. Freund, J. Peraire, and S. G. Johnson. Robust topology optimization of three-dimensional photonic-crystal band-gap structures. *Optics Express*, 22(19):22632, 9 2014. ISSN 1094-4087. doi: 10.1364/OE.22.022632. URL https://opg.optica.org/oe/abstract.cfm?uri=oe-22-19-22632.

[21] R. Mattoso, L. H. Gabrielli, and A. A. Novotny. Topology design optimization of nanophotonic devices for energy concentration. *Applied Mathematical Modelling*, 104:517–530, 2022. ISSN 0307-904X. doi: https://doi.org/10.1016/j.apm.2021.11.030. URL https://www.sciencedirect.com/science/article/pii/S0307904X21005655.

[22] F. Wang, R. E. Christiansen, Y. Yu, J. Mørk, and O. Sigmund. Maximizing the quality factor to mode volume ratio for ultra-small photonic crystal cavities. *Applied Physics Letters*, 113(24):241101, 12 2018. ISSN 0003-6951. doi: 10.1063/1.5064468. URL http://aip.scitation.org/doi/10.1063/1.5064468.

[23] R. E. Christiansen, F. Wang, J. Mørk, and O. Sigmund. Photonic cavity design by topology optimization. In B. Panchapakesan and A. Attias, editors, *Proceedings of SPIE - Nanoengineering: Fabrication, Properties, Optics, Thin Films, and Devices XVI*, volume 11089, pages 40–46. International Society for Optics and Photonics, SPIE, 2019. doi: 10.1117/12.2529099. URL https://doi.org/10.1117/12.2529099.

[24] F. Wang and O. Sigmund. Optimization of photonic crystal cavities. In *2017 International Conference on Numerical Simulation of Optoelectronic Devices (NUSOD)*, pages 39–40. IEEE, 7 2017. ISBN 978-1-5090-5323-0. doi: 10.1109/NUSOD.2017.8009980. URL http://ieeexplore.ieee.org/document/8009980/.

[25] J. S. Jensen and O. Sigmund. Topology optimization of photonic crystal structures: a high-bandwidth low-loss T-junction waveguide. *Journal of the Optical Society of America B*, 22(6):1191, 6 2005. ISSN 0740-3224. doi: 10.1364/JOSAB.22.001191. URL https://opg.optica.org/abstract.cfm?URI=josab-22-6-1191.

[26] P. I. Borel, A. Harpøth, L. H. Frandsen, M. Kristensen, P. Shi, J. S. Jensen, and O. Sigmund. Topology optimization and fabrication of photonic crystal structures. *Optics Express*, 12(9):1996, 5 2004. ISSN 1094-4087. doi: 10.1364/OPEX.12.001996. URL https://opg.optica.org/abstract.cfm?URI=oe-12-9-1996.

[27] F. Wang, J. S. Jensen, and O. Sigmund. Robust topology optimization of photonic crystal waveguides with tailored dispersion properties. *J. Opt. Soc. Am. B*, 28(3):387–397, 2011. doi: 10.1364/JOSAB.28.000387. URL http://josab.osa.org/abstract.cfm?URI=josab-28-3-387.

[28] Y. Chen, F. Meng, G. Li, and X. Huang. Topology optimization of photonic crystals with exotic properties resulting from Dirac-like cones. *Acta Materialia*, 164:377–389, 2019. ISSN 1359-6454. doi: https://doi.org/10.1016/j.actamat.2018.10.058. URL https://www.sciencedirect.com/science/article/pii/S1359645418308681.

[29] S. J. van den Boom, R. Abedi, F. van Keulen, and A. M. Aragón. On the importance of boundary smoothness in the computational design of phononic crystals. *Structural and Multidisciplinary Optimization*, 2021. doi: 10.1073/pnas.XXXXXXXXXX. URL www.pnas.org/cgi/doi/10.1073/pnas.XXXXXXXXXX.

[30] H. Hagino, Y. Takahashi, Y. Tanaka, T. Asano, and S. Noda. Effects of fluctuation in air hole radii and positions on optical characteristics in photonic crystal heterostructure nanocavities. *Physical Review B*, 79(8):085112, 2 2009. ISSN 1098-0121. doi: 10.1103/PhysRevB.79.085112. URL https://link.aps.org/doi/10.1103/PhysRevB.79.085112.

[31] T. Asano, B. S. Song, and S. Noda. Analysis of the experimental Q factors (˜ 1 million) of photonic crystal nanocavities. *Optics Express*, 14(5):1996, 2006. ISSN 1094-4087. doi: 10.1364/OE.14.001996. URL https://opg.optica.org/oe/abstract.cfm?uri=oe-14-5-1996.

[32] W. R. Frei and H. T. Johnson. Finite-element analysis of disorder effects in photonic crystals. *Physical Review B*, 70(16):165116, 10 2004. ISSN 1098-0121. doi: 10.1103/PhysRevB.70.165116. URL https://link.aps.org/doi/10.1103/PhysRevB.70.165116.

[33] N. Moës, J. Dolbow, and T. Belytschko. A finite element method for crack growth without remeshing. *International Journal for Numerical Methods in Engineering*, 46(1):131–150, 1999. ISSN 0029-5981. doi: 10.1002/(SICI)1097-0207(19990910)46:1⟨131::AID-NME726⟩3.0.CO;2-J. URL https://onlinelibrary.wiley.com/doi/10.1002/(SICI)1097-0207(19990910)46:1%3C131::AID-NME726%3E3.0.CO;2-J.

[34] C.A. Duarte, I. Babuška, and J.T. Oden. Generalized finite element methods for three-dimensional structural mechanics problems. *Computers & Structures*, 77(2):215–232, 6 2000. ISSN 00457949. doi: 10.1016/S0045-7949(99)00211-4. URL https://linkinghub.elsevier.com/retrieve/pii/S0045794999002114.

[35] N. Duan, W. Xu, S. Wang, H. Li, Y. Guo, and J. Zhu. Extended finite element method for electromagnetic fields. In *2015 IEEE International Conference on Applied Superconductivity and Electromagnetic Devices (ASEMD)*, pages 364–365. IEEE, 11 2015. ISBN 978-1-4673-8106-2. doi: 10.1109/ASEMD.2015.7453614. URL http://ieeexplore.ieee.org/document/7453614/.

[36] C. Siefert, T. E. Voth, and P. B. Bochev. Electromagnetic eXtended Finite Elements for Accurate Resolution of Multi-Material Cells. In *The ARL 2012 Research in Ballistic Protection Technologies Workshop*, United States, 2012. URL https://www.osti.gov/biblio/1117558.

[37] N. Duan, W. Xu, S. Wang, J. Zhu, and Y. Guo. An Improved XFEM With Multiple High-Order Enrichment Functions and Low-Order Meshing Elements for Field Analysis of Electromagnetic Devices With Multiple Nearby Geometrical Interfaces. *IEEE Transactions on Magnetics*, 51(3):1–4, 2015. ISSN 0018-9464. doi: 10.1109/TMAG.2014.2358792. URL http://ieeexplore.ieee.org/document/7093621/.

[38] N. Duan, W. Xu, S. Wang, and J. Zhu. Accuracy analysis of structure with nearby interfaces within XFEM. *AIP Advances*, 7(5):056011, 5 2017. ISSN 2158-3226. doi: 10.1063/1.4974983. URL http://aip.scitation.org/doi/10.1063/1.4974983.

[39] R. Adriano, W.G. Facco, and E. J. Silva. A Modified Plane Wave Enrichment to Solve 2-D Electromagnetic Problems Using the Generalized Finite-Element Method. *IEEE Transactions on Magnetics*, 51(3):1–4, 2015. ISSN 0018-9464. doi: 10.1109/TMAG.2014.2362102. URL http://ieeexplore.ieee.org/document/7093394/.

[40] S. Jeong, S. Lim, and S. Min. Level-Set-Based Topology Optimization Using Remeshing Techniques for Magnetic Actuator Design. *IEEE Transactions on Magnetics*, 52(3):1–4, 3 2016. ISSN 0018-9464. doi: 10.1109/TMAG.2015.2485260. URL http://ieeexplore.ieee.org/document/7286838/.

[41] S. J. van den Boom, J. Zhang, F. Keulen, and A. M. Aragón. A stable interface-enriched formulation for immersed domains with strong enforcement of essential boundary conditions. *International Journal for Numerical Methods in Engineering*, 120(10):1163–1183, 12 2019. ISSN 0029-5981. doi: 10.1002/nme.6139. URL https://onlinelibrary.wiley.com/doi/10.1002/nme.6139.

[42] S. J. van den Boom, F. van Keulen, and A. M. Aragón. Fully decoupling geometry from discretization in the Bloch–Floquet finite element analysis of phononic crystals. *Computer Methods in Applied Mechanics and Engineering*, 382:113848, 2021. ISSN 0045-7825. doi: 10.1016/j.cma.2021.113848. URL https://www.sciencedirect.com/science/article/pii/S0045782521001857.

[43] S. Soghrati, A. M. Aragón, C. Armando Duarte, and P. H. Geubelle. An interface-enriched generalized FEM for problems with discontinuous gradient fields. *International Journal for Numerical Methods in Engineering*, 89(8):991–1008, 2 2012. ISSN 00295981. doi: 10.1002/nme.3273. URL https://onlinelibrary.wiley.com/doi/10.1002/nme.3273.

[44] A. M. Aragón, B. Liang, H. Ahmadian, and S. Soghrati. On the stability and interpolating properties of the Hierarchical Interface-enriched Finite Element Method. *Computer Methods in Applied Mechanics and Engineering*, 362:112671, 2020. ISSN 0045-7825. doi: 10.1016/j.cma.2019.112671. URL https://www.sciencedirect.com/science/article/pii/S0045782519305560.

[45] K. Zhang, J. M. Jin, and P. H. Geubelle. A 3-D Interface-Enriched Generalized FEM for Electromagnetic Problems With Nonconformal Discretizations. *IEEE Transactions on Antennas and Propagation*, 63(12):5637–5649, 12 2015. ISSN 0018-926X. doi: 10.1109/TAP.2015.2489217. URL http://ieeexplore.ieee.org/document/7295572/.

[46] K. Zhang, A. R. Najafi, P. H. Geubelle, and J. M. Jin. A 2D interface-enriched generalized FEM for EM analysis of composite materials. In *2015 IEEE International Symposium on Antennas and Propagation & USNC/URSI National Radio Science Meeting*, volume 2015-Octob, pages 171–172. IEEE, 7 2015. ISBN 978-1-4799-7815-1. doi: 10.1109/APS.2015.7304471. URL http://ieeexplore.ieee.org/document/7304471/.

[47] K. Zhang, A. R. Najafi, P. H. Geubelle, and J. M. Jin. Gradient-based shape optimization for electromagnetic problems using IGFEM. In *2016 IEEE International Symposium on Antennas and Propagation (APSURSI)*, pages 579–580. IEEE, 2016. ISBN 978-1-5090-2886-3. doi: 10.1109/APS.2016.7695998. URL https://onlinelibrary.wiley.com/doi/10.1002/jnm.2073http://ieeexplore.ieee.org/document/7695998/.

[48] S. J. van den Boom, J. Zhang, F. van Keulen, and A. M. Aragón. An interface-enriched generalized finite element method for level set-based topology optimization. *Structural and Multidisciplinary Optimization*, 63(1):1–20, 1 2021. ISSN 1615-147X. doi: 10.1007/s00158-020-02682-5. URL http://link.springer.com/10.1007/s00158-020-02682-5.

[49] J. M. Jin. *The Finite Element Method in Electromagnetics*. John Wiley & Sons, 2nd editio edition, 2002.

[50] J. C. Nedelec. Mixed finite elements in ℝ3. *Numerische Mathematik*, 35(3):315–341, 9 1980. ISSN 0029-599X. doi: 10.1007/BF01396415. URL http://link.springer.com/10.1007/BF01396415.

[51] G. Mur. Edge Elements, their Advantages and their Disadvantages. *IEEE Transactions on Magnetics*, 30(5):3552–2557, 1994. doi: 10.1109/20.312706.

[52] R. E. Christiansen and O. Sigmund. Compact 200 line MATLAB code for inverse design in photonics by topology optimization: tutorial. *J. Opt. Soc. Am. B*, 38(2):510–520, 2 2021. doi: 10.1364/JOSAB.405955. URL http://opg.optica.org/josab/abstract.cfm?URI=josab-38-2-510.

[53] B. Hiett. *Photonic Crystal Modelling using Finite Element Analysis*. PhD thesis, University of Southampton, 2002.

[54] S. Koziel, X. Yang, and Q. Zhang. *Simulation-Driven Design Optimization and Modeling for Microwave Engineering*. Imperial College Press, 5 2013. ISBN 978-1-84816-916-6. doi: 10.1142/p860. URL https://www.worldscientific.com/worldscibooks/10.1142/p860.

[55] Ö. Özgün and M. Kuzuoğlu. *MATLAB®-based Finite Element Programming in Electromagnetic Modeling*. CRC Press, 9 2018. ISBN 9780429457395. doi: 10.1201/9780429457395. URL https://www.taylorfrancis.com/books/9780429854606.

[56] A. C. Polycarpou. Introduction to the Finite Element Method in Electromagnetics. *Synthesis Lectures on Computational Electromagnetics*, 1(1):1–126, 1 2006. ISSN 1932-1252. doi: 10.2200/S00019ED1V01Y200604CEM004. URL http://www.morganclaypool.com/doi/abs/10.2200/S00019ED1V01Y200604CEM004.

[57] J. M. Jin. *Theory and Computation of Electromagnetic Fields*. IEEE Press. Wiley, 2015. ISBN 9781119108047. URL https://books.google.nl/books?id=QOUxBwAAQBAJ.

[58] J. M. Jin and D. J. Riley. *Finite Element Analysis of Antennas and Arrays*. IEEE Press. Wiley, 2009. ISBN 9780470409725. URL https://books.google.nl/books?id=41MCAjp1SegC.

[59] K. Svanberg. The method of moving asymptotes—a new method for structural optimization. *International Journal for Numerical Methods in Engineering*, 24(2):359–373, 2 1987. ISSN 0029-5981. doi: 10.1002/nme.1620240207. URL https://onlinelibrary.wiley.com/doi/10.1002/nme.1620240207.

[60] C. A. Balanis. Advanced engineering electromagnetics, 1989. ISSN 2168-0329.

A

Sensitivity Analysis

The sensitivity to the optimization problem defined in Eq. 39 can be calculated with

$$\frac{\partial \Psi}{\partial d_i} = \frac{\partial \Psi}{\partial E_{zk}} \frac{\partial E_{zk}}{\partial \phi_j} \frac{\partial \phi_j}{\partial d_i}. \tag{49}$$

The first term is the derivative of the figure of merit with respect to the electric field values

$$\frac{\partial \Psi}{\partial E_{zk}} = -2 E^*_{zm} P_{mk}, \tag{50}$$

where $\bullet^*$ is the complex conjugate. The second term is the derivative of the electric field, with respect to every level set value, which can be calculated by first solving the linear equation

$$\left(\boldsymbol{M} - \omega^2 \boldsymbol{K}\right) \frac{\partial E^s_{zk}}{\partial \phi_j} = \left(\frac{\partial \boldsymbol{M}}{\partial \phi_j} - \omega^2 \frac{\partial \boldsymbol{K}}{\partial \phi_j}\right) E^s_{zk} - \boldsymbol{T} \left[\left(\frac{\partial \boldsymbol{M}}{\partial \phi_j} - \omega^2 \frac{\partial \boldsymbol{K}}{\partial \phi_j}\right) \bar{E}_{zk} + \left(\boldsymbol{M} - \omega^2 \boldsymbol{K}\right) \frac{\partial \bar{E}_{zk}}{\partial \phi_j} \right], \tag{51}$$

to find the derivative of the scattered field, after which the derivative of the incoming field can be added to get the the total field derivative with respect to every level set value. Here, $\bar{E}_z$ denotes the incoming electric field. The derivative of the system matrix with respect to a design variable can be calculated with

$$\frac{\partial \boldsymbol{M}}{\partial \phi_j} - \omega^2 \frac{\partial \boldsymbol{K}}{\partial \phi_j} = \sum_{l \in \iota_j} \sum_{e \in \iota l} \left(\frac{\partial \boldsymbol{m}_e}{\partial \boldsymbol{x}_l} - \omega^2 \frac{\partial \boldsymbol{k}_e}{\partial \boldsymbol{x}_l}\right) \frac{\partial \boldsymbol{x}_l}{\partial \phi_j}, \tag{52}$$

where ι_j is the set of enriched nodes which are influenced by the level set value ϕ_j, ι_l is the set of integration elements in the support of the enriched node $\boldsymbol{x}_l$ and

$$\frac{\partial \boldsymbol{x}_l}{\partial \phi_j} = -\frac{\phi(\boldsymbol{x}_k)}{\left(\phi(\boldsymbol{x}_j) - \phi(\boldsymbol{x}_k)\right)^2} \left(\boldsymbol{x}_j - \boldsymbol{x}_k\right), \tag{53}$$

which is the design velocities of enriched node $\boldsymbol{x}_l$, where $\boldsymbol{x}_j$ and $\boldsymbol{x}_j$ are the supporting nodes on the intersected edge from the original mesh. The term $\partial \bar{E}_{zk} / \partial \phi_j$ only has nonzero values in ι_j, which can be calculated by

$$\frac{\partial \bar{\alpha}_i}{\partial \boldsymbol{\phi_j}} = \sum_{l \in \iota_j} \left(\frac{\partial \bar{u}(\boldsymbol{x_i})}{\partial \boldsymbol{x}_l} \frac{\partial \boldsymbol{x}_l}{\partial \phi_j} - \sum_{j \in \iota_p} \frac{N_j(\boldsymbol{x_i})}{\partial \boldsymbol{x}_l} \frac{\partial \boldsymbol{x}_l}{\partial \phi_j} \bar{U}_j \right), \tag{54}$$

where the term $N_j(\boldsymbol{x_i}) / \partial \boldsymbol{x}_l$ is the change in shape function values at $\boldsymbol{x}_i$ when the enriched node moves and $\partial \bar{u}(\boldsymbol{x_i}) / \partial \boldsymbol{x}_l$ is the change in the incoming field value at $\boldsymbol{x}_i$ when the enriched node moves, which can be calculated by

$$\frac{\partial \bar{u}(\boldsymbol{x})}{\partial \boldsymbol{x}} = -j k_0 u_0 \exp\left[-j k_0 \left(x \cos \bar{\varphi} + y \sin \bar{\varphi}\right)\right] \begin{bmatrix} \cos \bar{\varphi} \\ \sin \bar{\varphi} \end{bmatrix}. \tag{55}$$

Note that the enriched node scaling $1/(s_i\psi_i(\boldsymbol{x}_i))$ that is present in Eq. 32 is set to 1 during optimization, hence why it is left out. Finally, the third term is the derivative of the nodal level set values with respect to the design variables, which is defined as

$$\frac{\partial \boldsymbol{\phi}}{\partial \boldsymbol{d}} = \boldsymbol{\theta}^{\mathrm{T}}. \tag{56}$$

Then we also check our analytical sensitivities by computing the absolute relative error with respect to finite difference sensitivities. The absolute relative error is defined as:

$$\delta_i = \frac{|\Psi_i' - \partial\Psi/\partial d_i|}{|\partial\Psi/\partial d_i|}, \tag{57}$$

where Ψ_i' is the sensitivity for node i calculated with the finite difference. This relative error was calculated for 5 non-zero design variables, the position of which are showed in Fig. 21. The resulting error shows the expected result where step sizes that are too large or small will result in a large error. For these 5 nodes, the optimal finite difference step size seems to be around $\Delta d_i = 1\mathrm{e}{-8}\,\mathrm{m}$.

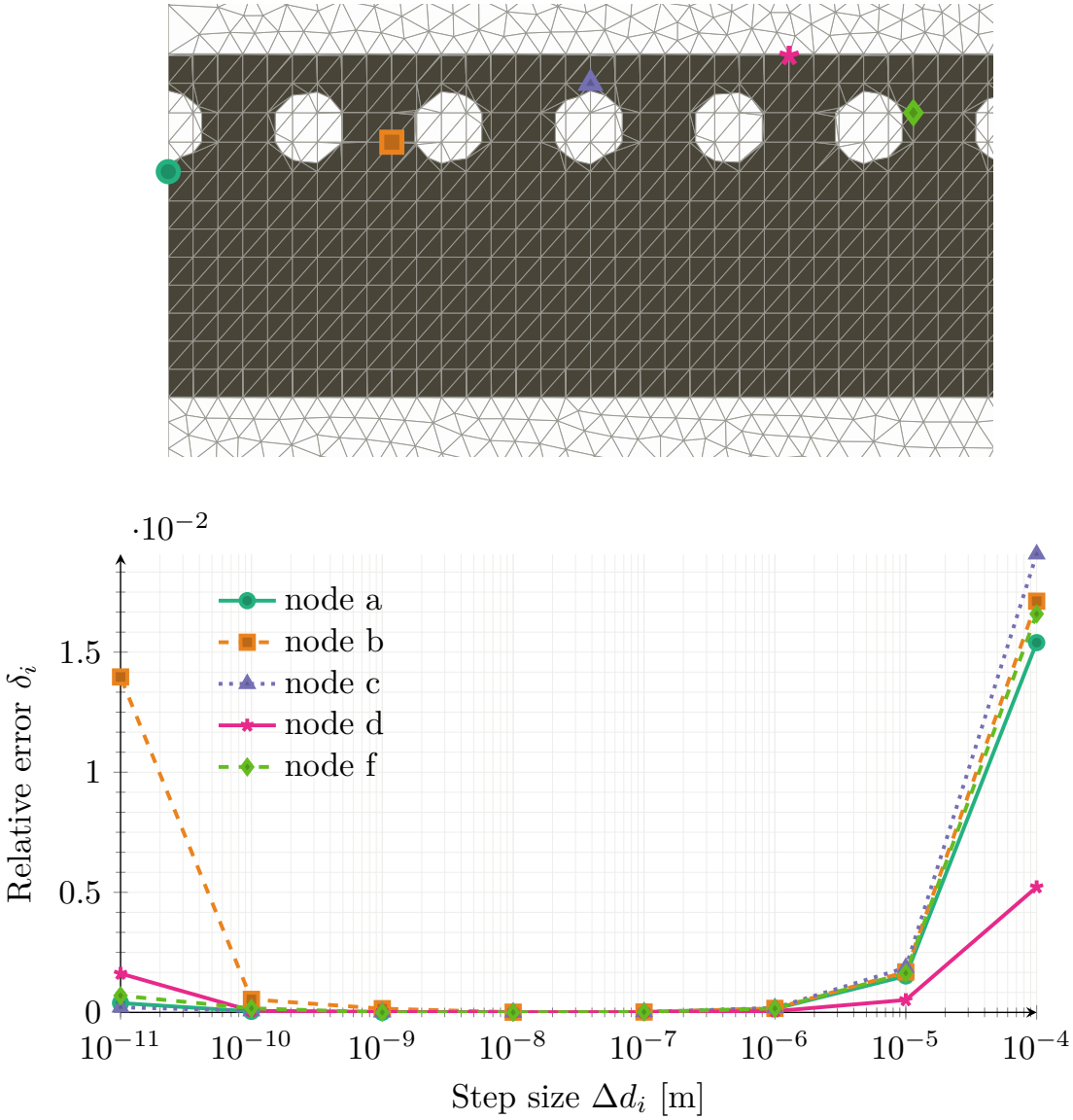

Fig. 21: The absolute relative error δ_i between sensitivities at 5 nodes calculated analytically or with a forward finite difference scheme for different step sizes Δd_i.